Bulk viscosity of stirred xenon near the critical point

K. A. Gillis, I. I. Shinder, and M. R. Moldover
Process Measurements Division, National Institute of Standards and Technology, Gaithersburg, Maryland 20899-8360, USA
(Received 18 April 2005; published 11 November 2005)

We deduce the thermophysical properties of near-critical xenon from measurements of the frequencies and half-widths of the acoustic resonances of xenon maintained at its critical density in centimeter-sized cavities. In the reduced temperature range $1\times10^{-3}<(T-T_c)/T_c<7\times10^{-6}$, we measured the resonance frequency and quality factor (Q) for each of six modes spanning a factor of 27 in frequency. As T_c was approached, the frequencies decreased by a factor of 2.2 and the Q's decreased by as much as a factor of 140. Remarkably, these results are predicted (within ±2% of the frequency and within a factor of 1.4 of Q) by a model for the resonator and a model for the frequency-dependent bulk viscosity $\zeta(\omega)$ that uses no empirically determined parameters. The resonator model is based on a theory of acoustics in near-critical fluids developed by Gillis, Shinder, and Moldover [Phys. Rev. E **70**, 021201 (2004)]. In addition to describing the present low-frequency data (from 120 Hz to 7.5 kHz), the model for $\zeta(\omega)$ is consistent with ultrasonic (0.4–7 MHz) velocity and attenuation data from the literature. However, the model predicts a peak in the temperature dependence of the dissipation in the boundary layer that we did not detect. This suggests that the model overestimates the effect of the bulk viscosity on the thermal boundary layer. In this work, the acoustic cavities were heated from below to stir the xenon, thereby reducing the density stratification resulting from Earth's gravity. The stirring reduced the apparent equilibration time from several hours to a few minutes, and it reduced the effective temperature resolution from 60 mK to approximately 2 mK, which corresponds to $(T-T_c)/T_c\approx7\times10^{-6}$.

DOI: 10.1103/PhysRevE.72.051201 PACS number(s): 51.40.+p, 64.70.Fx, 64.60.Ht, 51.10.+y

I. INTRODUCTION

In a previous publication [1], we determined accurate values of the isochoric heat capacity C_V and the thermal conductivity λ_T of near-critical xenon by measuring the frequencies and half-widths of acoustic resonances of Helmholtz cavity resonators filled with xenon at its critical density ρ_c. (For xenon, $T_c=16.58\ ^\circ$C, $P_c=5.84$ MPa, and $\rho_c=1116$ kg m^{-3}.) In that work, the analysis was restricted to large reduced temperatures $\tau\equiv(T-T_c)/T_c>1\times10^{-3}$ where $\omega t_\xi\ll1$ and the frequency-dependent bulk viscosity $\zeta(\omega)$ played a small role in the results. (Here, $\omega\equiv2\pi f$ is the angular frequency and t_ξ is the fluctuation relaxation time.) In this work, we extend the measurements and the analysis 140 times closer to the critical temperature to reach reduced temperatures as small as $\tau\approx7\times10^{-6}$, where $\zeta(\omega)$ dominates the dissipation. The measurements were accomplished by using thermally driven convection to stir the xenon inside the resonators. As T_c was approached, the Helmholtz mode of each resonator reached the condition $\omega t_\xi=1$ at the reduced temperature $\tau\approx2\times10^{-5}$. This is 100 times closer to T_c than previous work at megahertz frequencies [2–4]. Thus, the present results test dynamic scaling where the corrections to asymptotic behavior are expected to be small. Prior to this work, low-frequency acoustic measurements in near-critical fluids have been limited by (1) an incomplete theory of the resonators and (2) gravitational stratification. The first limit was addressed in Ref. [1]. In this work, we show that convective stirring virtually eliminates the second limit.

In pioneering work, Voronel showed that mechanical stirring reduces gravitational stratification of near-critical argon in a 10-cm-tall calorimeter. The stirring enabled him to make accurate heat-capacity measurements as close to T_c as $\tau\approx1\times10^{-4}$[5]. Mechanical stirring was used also during measurements of the attenuation and dispersion of sound in xenon near its critical point [2,3]. These measurements were made in tall cells and at high frequencies (0.4–7 MHz). In Sec. VI, we compare the ultrasonic measurements to the present results. Subsequently, Cannell [6] used a heater to force convective stirring in a 2-cm-tall optical cell filled with sulfur hexafluoride (SF_6) near its critical point. Cannell measured the intensity of the light scattered from a small volume in the center of the cell at reduced temperatures as small as $\tau=4\times10^{-6}$. The present work resembles Cannell's insofar as we stirred the xenon in our 2.3-cm-tall resonators by thermally driven convection. A key difference between this work and Cannell's is that the acoustic frequencies are sensitive to the thermodynamic state of the xenon throughout the volume of the cavity and the acoustic half-widths are particularly sensitive to the state of the xenon at the boundaries of the cavity. We assume that the stirring generated a nearly adiabatic temperature gradient throughout the volume and estimate in Sec. IV that the results have an effective resolution of $\tau\approx7\times10^{-6}$.

Substantial acoustic dissipation occurred at the walls of each resonator and throughout the volume of each resonator. In Ref. [1], we derived a model for the resonator from linear hydrodynamics that accounts for both the surface and the volume dissipation. Because calculations within this model become complicated near T_c, we performed them using two independent methods: (1) analytic solution of the damped wave equation and (2) treatment of the nonuniform surface admittance in perturbation theory. Both methods gave the same results.

A key input to the acoustic model is the frequency-dependent bulk viscosity $\zeta(\omega)$ that results from the relaxation

of critical fluctuations [7–9]. Theory does not provide a closed-form representation of $\zeta(\omega)$ for xenon (or any fluid with a nonzero background specific heat); therefore, we devised a function that interpolates between the theoretical low- and high-frequency limits of $\zeta(\omega)$. This interpolating function contains no parameters that could be fit to the present data. We tested the acoustic model and the function $\zeta(\omega)$ with our measurements of the resonance frequencies and the quality factors (Q) of six modes spanning a factor of 27 in frequency. As T_c was approached, in the reduced temperature range $1\times10^{-3}<\tau<7\times10^{-6}$, the frequencies decreased by a factor of 2.2 and the Q's decreased by as much as a factor of 140. Remarkably, the model predicts these results within ±2% of the frequency and within a factor of 1.4 of Q. A better approximation for $\zeta(\omega)$ might improve these results. The present model for $\zeta(\omega)$ describes the frequency dependence of the speed of sound at ultrasonic frequencies (0.4–7 MHz) as well as it described the present low-frequency data (from 120 Hz to 7.5 kHz). For any plausible form of $\zeta(\omega)$, the model predicts that the thermal penetration length becomes complex valued when $\gamma\omega t_\xi>1$. (Here, $\gamma\equiv C_P/C_V$ is the heat capacity ratio and C_P is the isobaric heat capacity.) Near $\gamma\omega t_\xi=1$, our model predicts a peak in the temperature dependence of the dissipation in the boundary layer that we did not detect. In our discussion of this discrepancy in Sec. VI, we conjecture that our model overestimates the role of the bulk viscosity on the thermal boundary layer dissipation.

In Sec. II, we describe the resonator's shape, its lowest-frequency acoustic modes, and the effects of gravitational stratification. Next, in Secs. III and IV we consider the thermal environment, convective stirring, and the determination of T_c. In Sec. V, we describe the acoustic model used in the analysis and, in Sec. VI, compare the predicted dissipation and dispersion with the data. In Sec. VI, we also discuss the consistency between the present model for $\zeta(\omega)$ and ultrasonic attenuation data (0.4–7 MHz) from the literature. In Sec. VII we list possible explanations for the small discrepancies between the measurements and the model.

II. RESONATOR, SPECTRUM, AND STRATIFICATION

This work extends the measurements described in Ref. [1] to smaller reduced temperatures. We used the same resonators and the same charges of xenon, but some of the thermistors used to record temperatures and temperature gradients were different than those used before. We did not carefully calibrate the thermistors used in the present work against a standard platinum resistance thermometer, because an accurate determination of T_c was not our objective. Thus, the difference between T_c reported here and T_c reported in Ref. [1] is due to the uncertainty in the thermistor calibration. No evidence of actual T_c drift was observed during the course of these or the previous measurements.

Figure 1 shows two cross sections of the resonator. The asymmetric design yields a spectrum (Fig. 2) with a low-frequency Helmholtz mode and five longitudinal modes that span a factor of 27 in frequency. Each of these six modes is well separated from all other modes. Reference [1] describes the resonator in more detail.

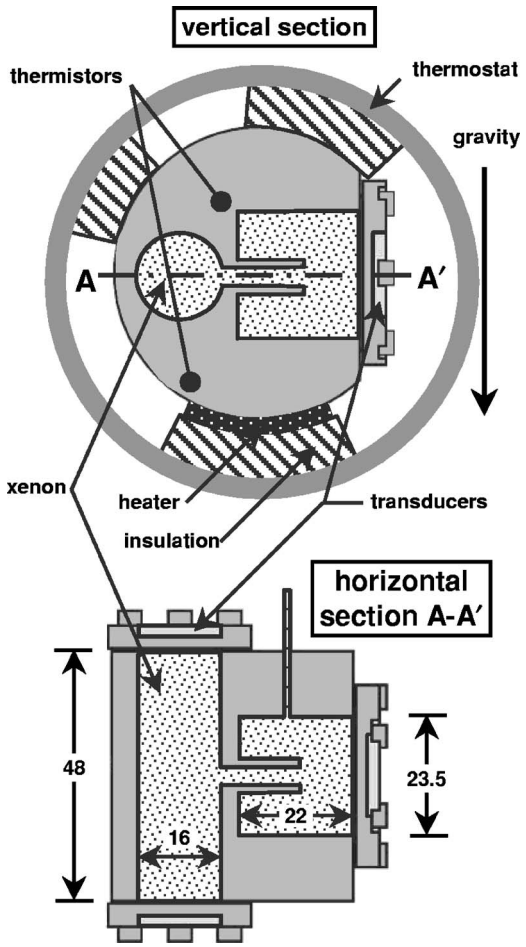

FIG. 1. Schematic cross sections of acoustic resonator and inner shell of thermostat. All dimensions are in mm. The duct's diameter was 4 mm and its length was 15 mm. The xenon-filled volume was 20 cm^3.

The xenon-filled volume consisted of two horizontal, cylindrical chambers; one was 48 mm long and 16 mm in diameter, and the other was 22 mm long and 23.5 mm in di-

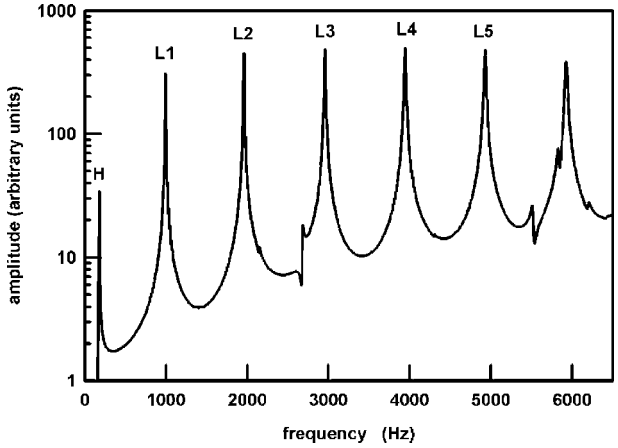

FIG. 2. Low-frequency acoustic modes of resonator filled with xenon at density ρ_c and reduced temperature $\tau=1\times10^{-3}$.

ameter. The chambers were oriented at right angles to each other and connected by a cylindrical duct 15 mm long and 4 mm in diameter. (See [1] for details.) Piezoelectric transducers were securely attached with epoxy to the outer sides of diaphragms (2.5 mm thick) machined into each end of the longer cylinder. One transducer was the driver; the second was the detector.

As discussed in [1], two nearly identical resonators were used. The internal surfaces of one resonator were coated with an 80-μm-thick layer of poly-monochloro-para-xylylene, a polymer known commercially as Parylene C [10]. The thermal impedance of the polymer layer is comparable to that of a layer of stainless steel 13 mm thick. (We use the value $\lambda_T = 0.0837$ W m^{-1} K^{-1} and $\varepsilon = 370$ kg K^{-1} s$^{-5/2}$ for the thermal conductivity and the effusivity of the polymer [11].)

Figure 2 displays the spectrum measured when the resonator was filled with xenon at its critical density and at the reduced temperature $\tau = 1 \times 10^{-3}$. The resonances that we studied are identified by H and $L1, \ldots, L5$. For the uncoated resonator, these modes had wave numbers $\omega/c \approx (12, 65, 130, 197, 261, \text{and } 326)$ m^{-1}. (c is the speed of sound.) The lowest-frequency resonance ($f_H \approx 120$ Hz near T_c) is the Helmholtz mode, in which the xenon oscillates between the two cylindrical chambers through the duct. In the lowest approximation, $(2\pi f_H)^2 \sim (\rho \kappa_S)^{-1}$, where κ_S is the adiabatic compressibility of the xenon averaged over both chambers and ρ is the density of the xenon in the duct [12]. The prominent resonances $L1, \ldots, L5$ are longitudinal modes in which the xenon oscillates parallel to the axis of the longer cylinder. Thus, the frequencies $f_{L1}, \ldots, f_{L5}$ depend only upon the speed of sound of the xenon in the longer chamber.

A detailed model for the resonance frequencies shows that they depend also upon the thermoacoustic boundary layers in the xenon at the solid surfaces of the resonator. Although these layers have thicknesses on the order of only 0.1–10 μm, they can change the frequencies by as much as 2.5%. Thus, accurate predictions of the resonance frequencies require knowledge of the temperature distribution on the surface of the resonator in addition to the temperature distribution throughout the interior of the resonator.

As T_c is approached, the xenon in an isothermal resonator becomes stratified in Earth's gravity [13,14]. Following Hohenberg and Barmatz [13], we numerically calculated the resonance frequencies of hypothetical resonators that have a rectangular cross section in vertical planes of height $h = 0$, 0.5, 1.4, 4, 12, and 32 mm and have their longest dimension in the horizontal plane. The calculations used estimates of the thermophysical properties of xenon based on our fit of the restricted cubic model [14] to high-quality experimental data from the literature [15–18]. The calculations assumed that the stratification was isothermal, and they neglected the boundary-layer corrections to the resonance frequencies. With these assumptions, the resonance frequencies of all the longitudinal modes (along the longest axis) changed by the same factor as a result of stratification, but there was a different factor for each resonator.

Figure 3 displays as smooth curves the calculated resonance frequencies divided by their values at $\tau = 1 \times 10^{-3}$. As T_c is approached, the calculated frequencies decrease, reach a shallow minimum at the temperature $\tau_{\min} = (9.38 \times 10^{-6})(h/\text{mm})^{0.639}$, and then increase.

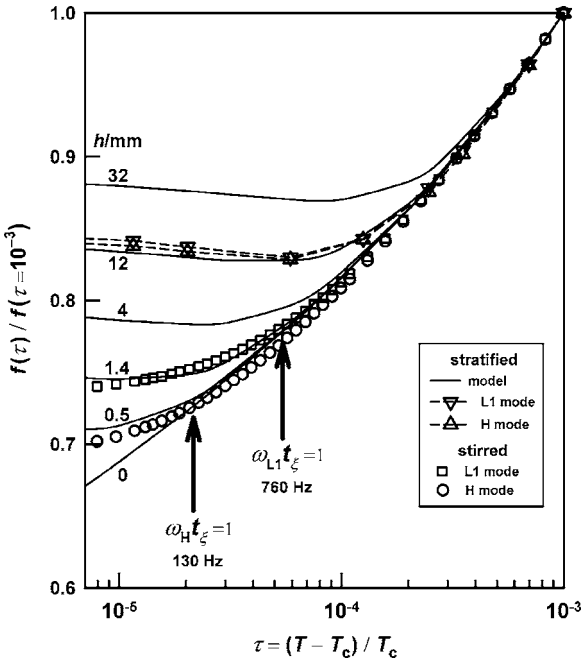

FIG. 3. Solid curves: calculated frequency ratios for the horizontally propagating, longitudinal modes of a rectangular cell of various heights (h) in millimeters. Triangles connected by the dashed curve: frequency ratios in the polymer-coated resonator in equilibrium under gravity. Isolated points: frequency ratios in the polymer-coated resonator measured while the xenon was stirred by convection.

Figure 3 also displays the frequency ratios measured in the isothermal resonator. (Here, we do not show data in the range $1 \times 10^{-3} < \tau < 1 \times 10^{-1}$; they are not influenced by stratification [1].) The frequency ratios for the H mode (triangles) are slightly larger than the ratios for the $L1$ mode (inverted triangles); both sets of ratios are close to the ratios calculated for a 12-mm-high cell with a rectangular cross section. The agreement is reasonable, considering that the measured f_{L1} depended upon the thermophysical properties of xenon averaged over a 16-mm-high circular cross section and the measured f_H depended upon an average over a more complicated volume 23.5 mm high.

For measurements near T_c, following a change in T, the mode frequencies required about 16 h to stabilize. This is the time required for an unstirred sample of xenon of this size to fully stratify.

To summarize, as expected in the absence of stirring, gravitational stratification limits the useful resolution of the acoustic measurements to $\tau > 2 \times 10^{-4}$, corresponding to $T - T_c > 60$ mK.

III. CONVECTIVE STIRRING

When near-critical fluids are heated from below, turbulent convection occurs whenever the magnitude of the vertical temperature gradient $|dT/dz|$ exceeds the magnitude of the adiabatic temperature gradient [14]:

$$-\frac{dT}{dz} > \rho g\left(\frac{\partial T}{\partial P}\right)_S. \quad (1)$$

(Here, the coordinate z is taken to increase upward and $g = 9.8\ m^2\ s^{-1}$ is the acceleration due to gravity.) A gradient of about $-1\ mK\ cm^{-1}$ is large enough to force convection in near-critical xenon. We note that discussions of Rayleigh-Benard convection in near-critical fluids [19,20] often add to the right-hand side of Eq. (1) the so-called Rayleigh term, which raises the convection threshold (due to dissipative processes) in geometries with a high degree of symmetry—e.g., a thin horizontal slab of fluid heated uniformly from below. As $T \to T_c$, this term decreases as $\tau^{1.87}$ and becomes smaller than the adiabatic gradient, which remains finite. We omitted the Rayleigh term from Eq. (1) because it is negligible compared to the adiabatic gradient for xenon in our temperature range and geometry [14].

We generated temperature gradients in the body of the resonator using a rectangular (25 mm × 50 mm), thin-film heater (134 Ω) glued to the bottom of the resonator near its center. As sketched in Fig. 1, three pieces of insulating foam held the resonator near the center of a cylindrical aluminum shell. The aluminum shell was the innermost shell of a four-stage air-filled thermostat that was maintained in a small refrigerator. (The thermostat has been described elsewhere [21].) When power was supplied to the heater, it generated a nonuniform temperature distribution in the steel cell. For example, the temperature difference between two thermistors embedded within the steel body of the polymer-coated resonator was 240 mK × ($\mathcal{P}$/W), where $\mathcal{P}$ was the power in watts dissipated in the heater (Fig. 1). A finite-element heat-transfer model suggested that similar temperature differences existed in the horizontal directions. One thermistor was approximately 3 cm higher than the other; thus, Eq. (1) suggests that 12 mW would be sufficient to exceed the adiabatic gradient. We interpret our experiments with different heater powers (discussed in the next section) to indicate that 8 mW was more than sufficient to stir the xenon, but 4 mW was marginal.

Our interpretation that the xenon is being convectively stirred is supported by the observation by Moldover *et al.* [14] that "convection cannot be avoided when a temperature gradient close to the adiabatic gradient is imposed on a near-critical fluid." Further support for this interpretation comes from theoretical evidence that oscillatory convective instabilities may occur in a near-critical fluid even when the temperature gradient is less than the adiabatic gradient [19].

The "stirred" data in Fig. 3 and the tabulated data were recorded using $\mathcal{P} \approx 8$ mW. The finite-element heat-transfer model suggested that the fluid was heated asymmetrically from the sides and bottom of the chambers. The temperature gradient within the bulk of the stirred xenon will be less than the gradient in the steel body of the resonator. By manipulating the set points of the thermostat shells, it was possible to measure the resonance frequencies while the resonator's average temperature was either held constant, increased, or decreased in a controlled fashion.

The heating had two effects on the xenon that were inferred from monitoring the resonance frequencies. First, the average temperature of the stirred xenon was colder than that indicated by the lower thermistor by 100 mK × ($\mathcal{P}$/W). This is illustrated for the Helmholtz mode in Fig. 4. Second, only about 1 min was required for the stirred xenon to reach a steady state following small temperature changes, either close to T_c or far above T_c. However, much longer times were required to achieve a steady state when the xenon was warmed from the coexisting liquid and vapor phases below T_c into a single phase above T_c.

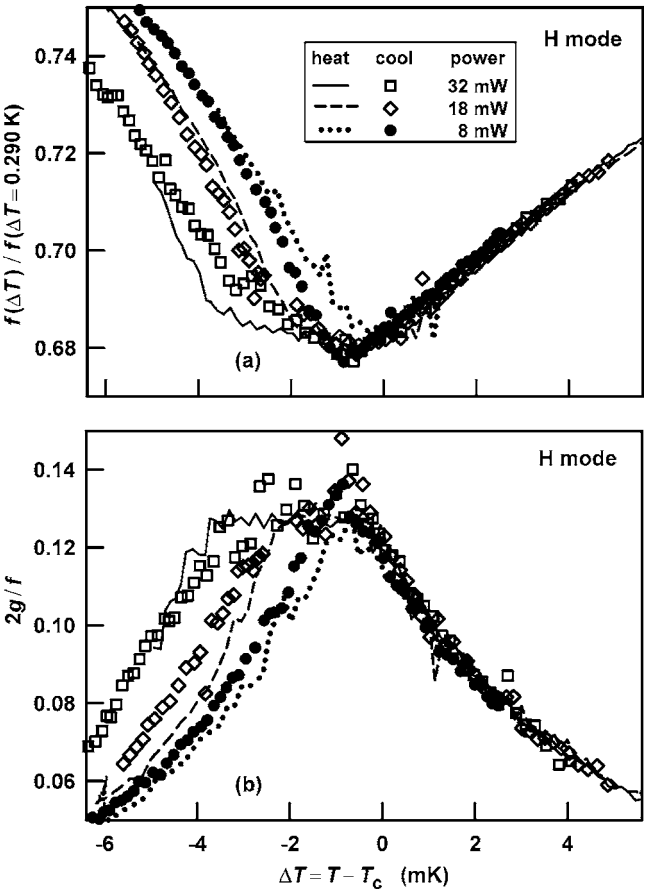

FIG. 4. (a) Frequency ratio and (b) dissipation ($2g/f$) data in the polymer-coated resonator for the Helmholtz mode near T_c for three heater powers. Before plotting, the data were shifted upward in temperature by 100 mK × [(heater power)/W].

The approach to a steady convective state, determined by relaxation of the viscous modes and sound modes, occurs on a short time scale (a few minutes), whereas the approach to thermal equilibrium occurs on the much longer time scale of the thermal relaxation time (a few hours) [14]. This supports our observations mentioned above. Therefore the convective state forms during a time in which the entropy remains constant, thus freezing in the adiabatic gradient. Based on these arguments and observations, we assume that the gradient within the stirred xenon is adiabatic. We do not know the actual density and temperature distributions from our measurements.

IV. DETERMINATION OF T_c

Figure 4 displays typical results near T_c. The frequencies f_H and the halfwidths g_H of the Helmholtz resonance are

plotted on a linear temperature scale. The frequencies are divided by 177.3 Hz, the value of f_H at $\tau=10^{-3}$, and the halfwidths are divided by $f_H/2$. (For the standard resonance formula, $2g/f=1/Q$, where Q is the "quality factor" of the resonance.) Six sets of data are plotted; they were acquired with 8, 18, and 32 mW supplied to the heater. For each heater power, data were acquired as the resonator cooled (plotted points) and warmed (jagged lines). Before plotting Fig. 4, the data were displaced toward higher temperatures by 100 mK$\times(\mathcal{P}/\mathrm{W})$. With this displacement, the six data sets coincide within ±0.2 mK at temperatures above T_c. This demonstrated that the results above T_c are independent of power applied to the heater. Below T_c, the warming and cooling data show hysteresis. The apparent equilibration time of the stirred xenon is much longer when it is in two phases below T_c than when it is in one phase above T_c. When the temperature was within ±5 mK of T_c, the data were equally spaced in temperature and acquired while the temperature was ramped at the rates of either +0.5 mK/h or −5 mK/h. Between T_c+5 mK and T_c+400 mK, the data were spaced logarithmically in temperature and acquired over a 10-h period. With these ramp rates and within this temperature range, the data acquired while warming and cooling were indistinguishable.

We also took data with $\mathcal{P}=4$ mW and similar warming and cooling rates. If they were plotted on Fig. 4, the cooling data would coincide with the higher-power data above T_c; the warming data were noisy and did not track the data at higher powers. This behavior suggests that 4 mW was insufficient to *reliably* stir the xenon. We interpret the difference in behavior between the 4-mW data and 8-mW data as signaling the onset of turbulent convection, although we did not detect it directly.

The data in Fig. 4 show one unexpected feature. When the stirring power was increased, the minimum value of the resonance frequency and the maximum value of the resonance half-width did not change significantly. However, their extent in temperature did increase. The "valley" in the upper panel of Fig. 4 acquires a flat bottom and the peak in the lower panel acquires a flat top. This flat top is especially clear for the other modes. (See Fig. 5.) We speculate that the width of this feature is determined by the width of the temperature distribution inside the stirred xenon. The width of this feature is only about a tenth of the temperature difference measured between the two thermistors embedded in the body of the resonator.

The onset of hysteresis described above coincided with the minimum in the frequency ratio for the 8-mW warming data in Fig. 4. The location of the minimum, as determined from a fit to the data in this region, differed by 0.2 mK or less for all modes observed with this power and ramp rate. We chose the average location of these minima as T_c and expressed the data as a function of reduced temperature. The two lower thermistors that were used in the present measurements are the same thermistors that Gillis *et al.* [1] used earlier. Between the two sets of measurements, these thermistors were removed from the cells, crudely recalibrated, sealed into the cell bodies with epoxy, and then compared to each other. This history leads us to recommend the value $T_c=16.583$ °C, for these samples of xenon, as reported in [1].

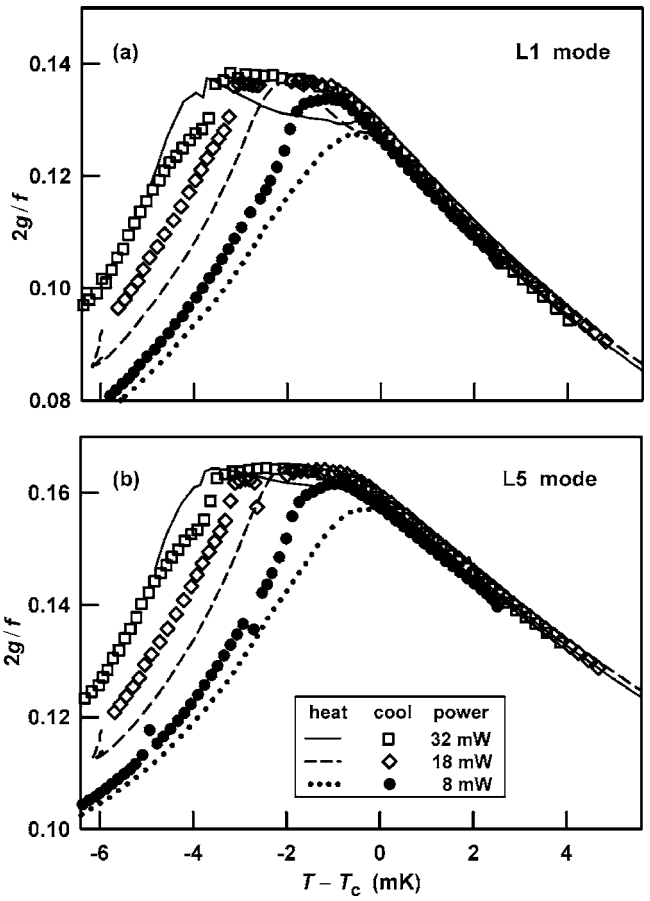

FIG. 5. Dissipation ($2g/f$) data in the polymer-coated resonator for the (a) $L1$ mode and (b) $L5$ mode near T_c for three heater powers. Before plotting, the data were shifted upward in temperature by 100 mK$\times$[(heater power)/W].

The resolution of the thermometry and of the acoustic measurements permitted measurements with a repeatability equivalent to approximately 0.2 mK (Figs. 4 and 5). However, the adiabatic temperature gradient in the stirred xenon was approximately 2 mK over its 2-cm height. This temperature difference corresponds to the reduced temperature $\tau \approx 7\times10^{-6}$. From the sensitivity of the dissipation and dispersion on reduced temperature, we estimate that the variation of the dissipation and dispersion across this temperature difference is at most 10% and 1.8%, respectively, at this lowest temperature. At $\tau\approx2\times10^{-4}$, these uncertainties drop to 0.4% and 0.2%, respectively. Because the acoustic measurements were determined by the properties averaged over this gradient, we restricted our analysis to data with $\tau>7\times10^{-6}$. The adiabatic density gradient as a result of stirring is much smaller than the isothermal gradient. Assuming that the gradient in our resonator is adiabatic, we estimate that the density deviation at $\tau\approx7\times10^{-6}$ spans the range $\pm3\times10^{-5}\rho_c$. The effect of this density variation on the acoustic measurements is negligible.

V. ACOUSTIC AND RESONATOR MODELS

The acoustic model used in the data analysis was based on the theory presented in Gillis, Shinder, and Moldover [1],

which was a generalization of a theory presented by Morse and Ingard [22]. The relationships between the pressure, temperature, and velocity fields developed in Gillis *et al.*, together with appropriate boundary conditions, were used to obtain a complete description of the Helmholtz and longitudinal modes of the resonator that included the thermal wave in the resonator wall, the effects of bulk viscosity, and an arbitrarily large heat capacity ratio γ. We argue that the theory is valid close to the liquid-vapor critical point (one-phase region), where the dissipation is large and the heat transport in the solid is significant. First, we specify the assumptions that underlie the model and derive expressions for propagating and evanescent waves; then, we specify the model for the bulk viscosity. With these tools, we calculate the resonance frequencies and half-widths.

A. Propagating and evanescent waves

The four scalar fields $\tilde{p}$, $\tilde{\rho}$, $\tilde{T}$, and $\tilde{s}$ and the vector field $\tilde{\mathbf{u}}$ represent the fluctuating pressure, density, temperature, entropy per unit mass, and (acoustic) fluid velocity, respectively; these fields are functions of position $\mathbf{r}$ and time t. We assume an implicit time dependence $e^{i\omega t}$ and that the amplitudes of the fluctuating fields $\tilde{p}$, $\tilde{\rho}$, $\tilde{T}$, and $\tilde{s}$ are small compared to their corresponding average values P, ρ, T, and S, respectively. The average fluid velocity is assumed to be zero, and the amplitude of $\tilde{\mathbf{u}}$ is assumed to be small compared to the speed of sound c. Near the critical point, we must further restrict the magnitudes of the fluctuating fields to be small compared to the average "distance" from the critical point—i.e., $\tilde{T} \ll (T-T_c)$, $\tilde{p} \ll (P-P_c)$, and $\tilde{\rho} \ll (\rho-\rho_c)$—to ensure that the sound wave does not influence the critical behavior.

We implicitly assume local thermodynamic equilibrium and appropriately impose no-slip, no-temperature-jump boundary conditions. To ensure local equilibrium, we require that the wavelength, the thicknesses of the boundary layers, and the dimensions of the resonator be larger than the correlation length or the mean free path, whichever is larger. As shown in Fig. 6, the boundary layer thicknesses δ_v and δ_T are an order of magnitude larger than the correlation length ξ for the ranges of frequency and reduced temperature τ spanned in this work. The mean free path for xenon at its critical density is about 3×10^{-10} m, which is much smaller than δ_v, δ_T, and ξ. Local equilibrium is therefore assured for the present work.

Theories for dynamics in critical phenomena [9] predict that critical fluctuations will be in equilibrium with an acoustically driven fluid as long as $\omega t_\xi \ll 1$. (t_ξ is the characteristic relaxation time for critical fluctuations.) In this limit, the transport coefficients and thermodynamic functions obey the static scaling laws. When $\omega t_\xi \geq 1$, the fluctuations cannot keep up with the acoustic oscillation. As a result, the bulk viscosity $\zeta(\omega)$, shear viscosity $\eta(\omega)$, and thermal conductivity $\lambda_T(\omega)$ become complex-valued, frequency-dependent functions that saturate at frequency-dependent values instead of diverging as $\tau \to 0$. The frequency dependences of these transport coefficients lead to dispersion and increased attenuation of sound waves.

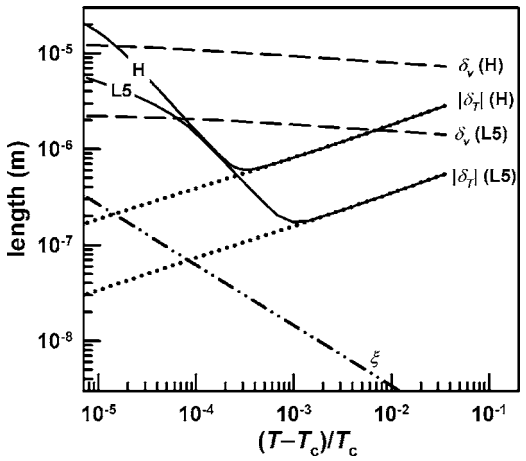

FIG. 6. Comparison of lengths as functions of the reduced temperature τ. The viscous penetration length δ_v and the thermal penetration length magnitude $|\delta_T|$ are shown for the lowest and highest-frequency modes H and $L5$, respectively. The dotted lines are predicted by $(2D_T/\omega)^{1/2}$. ξ is the correlation length. The mean free path is approximately 3×10^{-10} m; thus, it is much smaller than the plotted lengths.

Since the thermal dissipation and shear dissipation are much smaller than the dissipation from bulk viscosity, we neglected the frequency dependences of the shear viscosity [23] and thermal conductivity in our calculations. This approximation for the shear viscosity introduced a maximum error in the calculated dissipation of only 0.03%, which occurred at $\tau \approx 7\times10^{-6}$ for the Helmholtz mode in the steel resonator. The error from the thermal conductivity is not so easily determined. To our knowledge, a dynamic scaling function for $\lambda_T(\omega)$ has never been published. By analogy with the shear viscosity, we assumed $\lambda_T(\tau,\omega) = \lambda_T(\tau, 0)[S(-i\omega t_\xi/2)]^{-x_\lambda/z}$, where the dynamic scaling function S was developed for $\eta(\omega)$ in Ref. [23], $x_\lambda \approx 0.90$ is the scaling exponent for $\lambda_T \sim \xi^{x_\lambda}$, and $z \approx 3.069$ is the dynamic exponent. With these assumptions, we estimate that using the static thermal conductivity introduced a maximum error in the calculated dissipation of 1% at $\tau \approx 7\times10^{-6}$ for the Helmholtz mode in the steel resonator.

We do consider the bulk viscosity $\zeta(\omega)$ to be a complex-valued function of ω that is determined by the dynamic theory of critical phenomena. The thermodynamic properties (speed of sound, c, specific heat C_V, etc.) that appear in the equations below are the zero-frequency properties unless specified otherwise. However, we show how the inclusion of $\zeta(\omega)$ in the basic hydrodynamic equations leads to the frequency-dependent sound speed $c(\omega)$, specific heat $C_V(\omega)$, and adiabatic compressibility $\kappa_S(\omega)$ as discussed by others [7,9].

In Ref. [1], we assumed that linear acoustics was sufficient to describe our measurements. Here, we tested this assumption by performing additional measurements at $T-T_c = 0.01$, 0.1, 0.4, and 6 K. We varied the drive level by a factor of 100 and found that the acoustic pressure was a linear function of the drive level. Furthermore, there was no detectable change in the resonance frequency or the Q. Finally, we detected no harmonics of the drive frequency.

Therefore, we omitted the second-order (and higher) terms from the equations of motion, continuity, and entropy [22,9] because they lead to nonlinear solutions and amplitude-dependent dissipation. We estimate that omission of the viscous stress term from the entropy is justified as long as the acoustic pressure is much less than 2×10^4 Pa at $\tau=3\times10^{-4}$ and much less than 20 Pa at $\tau=1\times10^{-5}$. Based on the measured transducer sensitivity, the acoustic pressure in our resonator was about 100 Pa at $\tau=3\times10^{-4}$ and less than 5 Pa at $\tau=1\times10^{-5}$ for the acoustic measurements presented in Sec. VI.

The effect of fluid motion (stirring) on acoustic wave propagation and dissipation is proportional to M^2, where M is the Mach number (fluid speed)/(sound speed) [22]. Therefore the effects will be very small until the flow speed is a substantial fraction of the speed of sound. If M were not small, our results would have shown a strong dependence on the applied heater power, which we show was not the case.

The linearized forms of the Navier-Stokes (NS) equation, the continuity equation, the diffusion equation for heat flow (in the fluid and in the wall), and the thermodynamic relationships between the fluctuating fields describe the basic physics. After we decompose the fluid velocity $\tilde{\mathbf{u}}$ into the sum $\tilde{\mathbf{u}}_1+\tilde{\mathbf{u}}_{\rm vor}$ of the curl-free ($\boldsymbol{\nabla}\times\tilde{\mathbf{u}}_1=\mathbf{0}$) and divergence-free ($\boldsymbol{\nabla}\cdot\tilde{\mathbf{u}}_{\rm vor}=0$) parts, replace $\partial/\partial t$ with $i\omega$, and eliminate $\tilde{s}$ and $\tilde{\rho}$, the equations for the fluid become

$$\tilde{\mathbf{u}}=\tilde{\mathbf{u}}_1+\tilde{\mathbf{u}}_{\rm vor}, \tag{2a}$$

$$\text{(curl-free NS)}\quad i\omega\rho\tilde{\mathbf{u}}_1=-\boldsymbol{\nabla}\tilde{p}+\left(\zeta(\omega)+\frac{4}{3}\eta\right)\nabla^2\tilde{\mathbf{u}}_1, \tag{2b}$$

$$\text{(divergence-free NS)}\quad i\omega\rho\tilde{\mathbf{u}}_{\rm vor}=\eta\nabla^2\tilde{\mathbf{u}}_{\rm vor}, \tag{2c}$$

$$\text{(continuity)}\quad i\omega\beta_P\tilde{T}-i\omega\kappa_T\tilde{p}=\boldsymbol{\nabla}\cdot\tilde{\mathbf{u}}_1, \tag{2d}$$

$$\text{(heat flow)}\quad i\omega\rho C_P\tilde{T}-i\omega\beta_P T\tilde{p}=\lambda_T\nabla^2\tilde{T}, \tag{2e}$$

where κ_T is the isothermal compressibility, β_P is the isobaric expansivity, C_P is the isobaric heat capacity per unit mass, and λ_T is the thermal conductivity.

The acoustic wave within the rigid solid is neglected. However, the temperature distribution in the solid must not be neglected near the fluid's critical point. As $\tau\to0$ the heat capacity per unit area in the fluid's boundary layer exceeds the heat capacity per unit area in the solid's boundary layer, so heat driven into the solid will cause substantial temperature gradients there. The equation for heat transfer in the solid is

$$\nabla^2\tilde{T}_s=(i\omega\rho_sC_{Ps}/\lambda_{Ts})\tilde{T}_s=-k_{Ts}^2\tilde{T}_s. \tag{3}$$

The subscript s is used to identify the solid (bare steel or polymer in our case) unless stated otherwise. Since k_{Ts}^2 is purely imaginary, Eq. (3) describes a diffusive thermal wave with wave number $k_{Ts}=(1-i)/\delta_{Ts}$ and thermal penetration length $\delta_{Ts}=\sqrt{2\lambda_{Ts}/(\omega\rho_sC_{Ps})}$.

Equations (2) and (3) must be solved for the resonator geometry subject to the boundary conditions on the fluid velocity ($\tilde{\mathbf{u}}=\tilde{\mathbf{u}}_1+\tilde{\mathbf{u}}_{\rm vor}$) and the temperature

$$|\tilde{\mathbf{u}}_\perp(\mathbf{r}_w)|=0\quad\text{(rigid wall)}, \tag{4a}$$

$$|\tilde{\mathbf{u}}_\parallel(\mathbf{r}_{\rm w})|=0\quad\text{(no slip)}, \tag{4b}$$

$$\tilde{T}(\mathbf{r}_{\rm w})=\tilde{T}_s(\mathbf{r}_{\rm w})\quad\text{(local equilibrium)}, \tag{4c}$$

$$[\lambda_T\nabla_\perp\tilde{T}(\mathbf{r}_{\rm w})]=[\lambda_T\nabla_\perp\tilde{T}(\mathbf{r}_{\rm w})]_s\quad\text{(energy conservation)}. \tag{4d}$$

The vector $\mathbf{r}_{\rm w}$ locates a point on the resonator wall. The subscript $\perp$ and $\parallel$ designate, respectively, vector components perpendicular to and parallel to the wall.

As the Appendix of Ref. [1] explains, the system of equations (2) supports one propagating mode (the acoustic wave) and two diffusing modes (thermal and shear waves). The acoustic wave is a long-wavelength oscillation that, in an unbounded system, can travel many wavelengths before being significantly damped. The thermal and shear waves are diffusion modes that arise due to heat and momentum transfer, respectively, between adjacent portions of the fluid. These modes do not propagate; instead, they are exponentially damped over a distance that is orders of magnitude smaller than the acoustic wavelength at the same frequency. The diffusion modes are important near boundaries where the acoustic wave alone cannot satisfy all the boundary conditions. This coupling through the boundary conditions between the acoustic and diffusion wave modes is an important mechanism that dissipates acoustic energy. Here, we describe in detail how the predicted nature of these modes near the liquid-vapor critical point differs from classical acoustics.

The acoustic pressure is a solution of $\nabla^2\tilde{p}_{\rm ac}=-k_{\rm ac}^2\tilde{p}_{\rm ac}$, where the dispersion relation is

$$k_{\rm ac}^2=\frac{\omega^2}{c^2}q_-^2(\omega), \tag{5}$$

with

$$q_-^2(\omega)=\frac{2}{1+i\Delta_{\rm v}+i\gamma\Delta_T+\Xi}, \tag{6}$$

$$\Delta_{\rm v}=\frac{\omega}{c^2}\left(\frac{\zeta(\omega)}{\rho}+\frac{4}{3}D_{\rm v}\right),\quad \Delta_T=\frac{\omega}{c^2}D_T, \tag{7}$$

and

$$\Xi^2=(1+i\Delta_{\rm v}-i\gamma\Delta_T)^2+4i\Delta_T(\gamma-1). \tag{8}$$

The viscous diffusivity (or kinematic viscosity) $D_{\rm v}=\eta/\rho$ and the thermal diffusivity $D_T=\lambda_T/(\rho C_P)$ are used for brevity. For a freely propagating damped acoustic wave, we usually write $k_{\rm ac}=[\omega/c(\omega)][1-i\alpha_\lambda/(2\pi)]$, where the phase velocity is $c(\omega)=\omega/{\rm Re}(k_{\rm ac})$ and the attenuation per wavelength is $\alpha_\lambda=-2\pi\,{\rm Im}(k_{\rm ac})/{\rm Re}(k_{\rm ac})$. The dispersion relation, Eq. (5), gives explicitly the frequency dependence of the phase velocity in terms of the transport coefficients. We can also write

the phase velocity and the attenuation in terms of $q_-(\omega)$, from Eq. (6), as

$$c(\omega) = \frac{c}{\mathrm{Re}[q_-(\omega)]} \tag{9}$$

and

$$\alpha_\lambda = \frac{2\pi\,\mathrm{Im}[q_-(\omega)]}{\mathrm{Re}[q_-(\omega)]}, \tag{10}$$

respectively. If this free-space attenuation were the only damping, then the quality factor of an acoustic resonance in a chamber would be $Q=\pi/\alpha_\lambda$.

The temperature, density, and velocity fields for the acoustic wave are

$$\tilde{T}_{\mathrm{ac}} = \frac{\gamma-1}{\gamma\bar{\alpha}}\frac{T_c}{P_c}\frac{\tilde{p}_{\mathrm{ac}}}{1-i\Delta_T q_-^2}, \tag{11}$$

$$\tilde{\rho}_{\mathrm{ac}} = \frac{q_-^2}{1-i\Delta_v q_-^2}\frac{\tilde{p}_{\mathrm{ac}}}{c^2}, \tag{12}$$

and

$$\tilde{\mathbf{u}}_{\mathrm{ac}} = -\frac{1}{1-i\Delta_v q_-^2}\frac{\boldsymbol{\nabla}\tilde{p}_{\mathrm{ac}}}{i\omega\rho}. \tag{13}$$

The dimensionless quantity $\bar{\alpha}\equiv(T_c/P_c)(\partial P/\partial T)_\rho$ is finite and continuous at the critical point: $\bar{\alpha}\approx 6$ at the critical point for xenon [17].

The temperature of the thermal wave is a solution of $\nabla^2\tilde{T}_T=-k_T^2\tilde{T}_T$, where

$$k_T^2 = \frac{\omega^2}{c^2}q_+^2(\omega) = \frac{\omega}{2D_T}\left[\frac{1+i\Delta_v+i\gamma\Delta_T+\Xi}{i(1+i\gamma\Delta_v)}\right] \tag{14}$$

and

$$q_+^2(\omega) = \frac{1+i\Delta_v+i\gamma\Delta_T+\Xi}{2i\Delta_T(1+i\gamma\Delta_v)}. \tag{15}$$

The thermal penetration length δ_T, defined such that $k_T^2=-2i/\delta_T^2$, is given by

$$\delta_T \equiv \frac{1-i}{k_T} = \left(\frac{2D_T}{\omega}\right)^{1/2}\left[\frac{2(1+i\gamma\Delta_v)}{1+i\Delta_v+i\gamma\Delta_T+\Xi}\right]^{1/2}. \tag{16}$$

The pressure, density, and velocity fields for the thermal wave are

$$\tilde{p}_T = \frac{\gamma\bar{\alpha}}{\gamma-1}\frac{P_c}{T_c}(1-i\Delta_T q_+^2)\tilde{T}_T, \tag{17}$$

$$\tilde{\rho}_T = \frac{\gamma\bar{\alpha}}{\gamma-1}\frac{P_c}{T_c}\frac{1-i\Delta_T q_+^2}{1-i\Delta_v q_+^2}\frac{q_+^2}{c^2}\tilde{T}_T, \tag{18}$$

and

$$\tilde{\mathbf{u}}_T = -\frac{\gamma\bar{\alpha}}{\gamma-1}\frac{P_c}{T_c}\frac{1-i\Delta_T q_+^2}{1-i\Delta_v q_+^2}\frac{1}{i\omega\rho}\boldsymbol{\nabla}\tilde{T}_T, \tag{19}$$

respectively.

Over the frequency and temperature ranges in this work—i.e., $f<10$ kHz and $2\times10^{-6}<\tau<0.04$—Δ_T and $\gamma\Delta_T$ are always much smaller than unity.[1] Although Δ_v and $\gamma\Delta_v$ are much smaller than unity far from the critical point, these quantities rapidly grow as T approaches T_c (due to the scaling behavior of ζ and γ) and must not be neglected. The approximations

$$\delta_T \approx \left(\frac{2D_T}{\omega}\right)^{1/2}\left[\frac{(1+i\Delta_v)(1+i\gamma\Delta_v)}{(1+i\Delta_v)^2+i(\gamma-1)\Delta_T}\right]^{1/2} \tag{20}$$

and

$$k_{\mathrm{ac}} \approx \frac{\omega}{c}\left[\frac{1+i\Delta_v}{(1+i\Delta_v)^2+i(\gamma-1)\Delta_T}\right]^{1/2} \tag{21}$$

are valid for a wide range of temperatures and frequencies. Outside the critical region, where $\gamma\Delta_v$ and $\gamma\Delta_T$ are both very much smaller than 1, Eqs. (20) and (21) reduce to

$$\delta_T \approx \left(\frac{2D_T}{\omega}\right)^{1/2}[1+i(\gamma-1)(\Delta_T-\Delta_v)]^{-1/2} \tag{22}$$

and

$$k_{\mathrm{ac}} \approx \frac{\omega}{c}[1+i\Delta_v+i(\gamma-1)\Delta_T]^{-1/2} \tag{23}$$

to lowest order in Δ_T and Δ_v. In the limit that $\gamma\Delta_v$ and $\gamma\Delta_T$ are completely negligible, Eq. (22) reduces to the classical expression for the thermal penetration length $\sqrt{2D_T/\omega}$. Close to the critical point, where $|\Delta_v|\approx 0.1$ and $\gamma|\Delta_v|\gg 1$, but still $\gamma\Delta_T\ll 1$, the approximations are

$$\delta_T \approx \left(\frac{2D_T}{\omega}\right)^{1/2}\left(\frac{i\gamma\Delta_v}{1+i\Delta_v}\right)^{1/2} \tag{24}$$

and

$$k_{\mathrm{ac}} \approx \frac{\omega}{c}\frac{1}{(1+i\Delta_v)^{1/2}}. \tag{25}$$

In this limit the dispersion relation Eq. (25) can be written as

$$\frac{\omega^2}{k_{\mathrm{ac}}^2} = c^2 + \frac{i\omega\zeta(\omega)}{\rho} + \frac{4}{3}\frac{i\omega\eta(\omega)}{\rho}, \tag{26}$$

which is consistent Onkui's Eqs. (5.4.25) and (6.2.23) in Ref. [9]. The shear-viscosity term is negligible in this limit. Following Onuki, Eq. (26) may also be written in terms of a frequency-dependent adiabatic compressibility—i.e., $\omega^2/k_{\mathrm{ac}}^2=1/\rho\kappa_S(\omega)$, where

[1] At the temperature and frequency extremes of this work, $\tau=1\times10^{-5}$ and 10 kHz, $\gamma\Delta_T\approx 2\times10^{-7}$. At sufficiently high frequency and low reduced temperatures, $\gamma\Delta_T$ should approach 1. However, at $\tau=1\times10^{-7}$ and 1 MHz, we estimate $\gamma\Delta_T$ will be just 0.02.

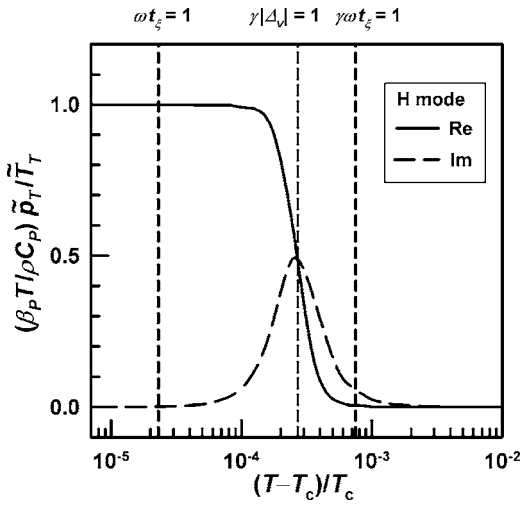

FIG. 7. The real and imaginary parts of $(\beta_P T/\rho C_P)\tilde{p}_T/\tilde{T}_T$ for the H mode as a function of reduced temperature. See discussion near Eq. (28).

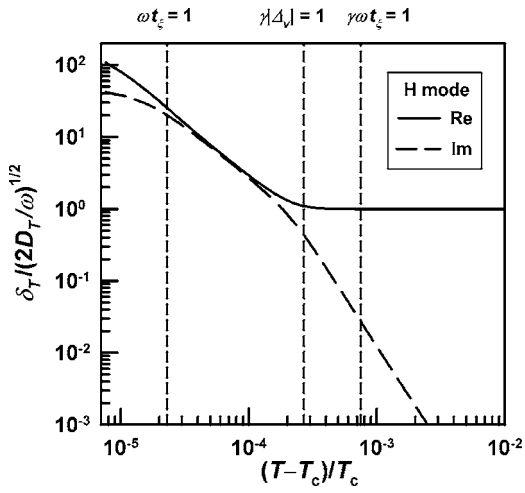

FIG. 8. Real and imaginary parts of $\delta_T/(2D_T/\omega)^{1/2}$ from Eq. (16) for the H mode as a function of reduced temperature.

$$\kappa_S(\omega) = \frac{\kappa_S}{1 + \dfrac{i\omega\zeta(\omega)}{\rho c^2} + \dfrac{4}{3}\dfrac{i\omega\eta(\omega)}{\rho c^2}}. \tag{27}$$

The agreement between these relations and the formal dynamic theory supports the basic assumptions of the model presented here.

The complex forms of k_{ac} and δ_T arise naturally from the coupled system of equations (2). Indeed, the presence of the complex-valued factor on the right-hand side of Eq. (16) for δ_T is a remnant of the pressure term in Eq. (2e). This term describes the entropy change due to an isothermal change in pressure. The relative importance of the pressure term in Eq. (2e) for the thermal wave is determined by the ratio

$$\frac{\beta_P T}{\rho C_P}\frac{\tilde{p}_T}{\tilde{T}_T} = 1 - i\Delta_T q_+^2, \tag{28}$$

which follows from Eq. (17). Outside the critical region, the thermal wave pressure $\tilde{p}_T$ is negligible because $|1-i\Delta_T q_+^2| \approx (\gamma-1)(\Delta_v-\Delta_T) \ll 1$ and Eq. (2e) reduces to the ordinary diffusion equation with the classical penetration length. Inside the critical region, $|1-i\Delta_T q_+^2|$ grows as $\tau\to 0$, it becomes non-negligible when $\gamma\omega t_\xi \approx 1$, and it is nearly unity when $\gamma|\Delta_v| \approx 1$. This behavior of $|1-i\Delta_T q_+^2|$ estimated from our model for the H mode is shown graphically as a function of τ in Fig. 7. Note that for $\gamma\Delta_v > 1$ (to the left of the central dashed line in Fig. 7), the two terms on the left-hand side of Eq. (2e) very nearly cancel, so the entropy of the thermal wave becomes negligible.

As $\tau\to 0$ the increasing importance of the thermal wave pressure is accompanied by a change in the spatial profile of the thermal wave because $\mathrm{Im}[\delta_T]$ is increasing and the wave number k_T is becoming purely imaginary. The behavior of δ_T for the H mode as a function of reduced temperature is shown in Fig. 8. The imaginary part of δ_T grows as $\tau\to 0$, it becomes non-negligible when $\gamma\omega t_\xi \approx 1$, and it is nearly equal to the real part when $\gamma|\Delta_v| \approx 1$.

The other diffusion mode is the shear (or vorticity) wave. This mode has just one field (the shear velocity $\tilde{\mathbf{u}}_{vor}$) that satisfies $\nabla^2\tilde{\mathbf{u}}_{vor} = -\boldsymbol{\nabla}\times(\boldsymbol{\nabla}\times\tilde{\mathbf{u}}_{vor}) = -k_v^2\tilde{\mathbf{u}}_{vor}$, where $k_v^2 = -2i/\delta_v^2$. The viscous penetration length $\delta_v = \sqrt{2\eta/(\rho\omega)}$ is real, since the coefficient of shear viscosity η is assumed here to be real and frequency independent. Although near-critical fluids are known to be weakly viscoelastic due to the slowly relaxing critical fluctuations [9,23], the effect is small and completely negligible in the context considered here. However, for situations in which the dissipation from bulk viscosity is negligible, such as the shear viscosity measurements in near-critical xenon by Berg *et al.* [24], viscoelastic effects may play a dominant role. If the viscoelastic effects are retained, then η and, therefore, δ_v become complex valued when $\omega t_\xi > 1$. In the high-frequency limit, where viscoelastic effects are largest, the theory of critical dynamics predicts that the ratio $-\mathrm{Im}[\eta(\omega)]/\mathrm{Re}[\eta(\omega)]$ is less than about 0.04. Therefore $|\mathrm{Im}(\delta_v)/\mathrm{Re}(\delta_v)|$ is always much less than 1, in contrast to the complex-valued thermal penetration length that we discuss above.

B. Bulk viscosity

Onuki [9] derives an integral expression for the frequency-dependent bulk viscosity that includes the correction for the background specific heat. To our knowledge, neither an analytic nor a numeric evaluation of the integral has been published, except for specific limiting cases. Onuki evaluates the bulk viscosity in the low and high-frequency limits. In the low-frequency limit ($\omega t_\xi \ll 1$), the bulk viscosity behaves as

$$\frac{i\omega\zeta(0)}{\rho c^2} = \frac{R_B i\omega t_\xi}{1+q_B}, \tag{29}$$

where $t_\xi = 6\pi\xi^3\eta/(k_B T_c) = t_0\tau^{-\nu z}$ is the fluctuation relaxation time, z is the dynamic exponent, and R_B is a universal number. Measurements of low-frequency sound attenuation in ^{3}He suggest $R_B \approx 0.03$ [3]. The nonuniversal parameter q_B is

the ratio between the background and singular parts of the reduced specific heat [1,9]—i.e.,

$$q_{\mathrm{B}} = \frac{C^*_{V,\mathrm{background}}}{C^*_{V,\mathrm{singular}}} = \frac{C^*_V}{A^+\tau^{-\alpha}} - 1, \tag{30}$$

where $C^*_V = T_c\rho_c C_V / P_c \approx A^+\tau^{-\alpha} + B^+$ is the reduced specific heat, A^+ is the universal specific heat amplitude, and B^+ is the nonuniversal background. For xenon, we use $A^+ = 18.015$ and $B^+ = -18.043$, as determined in Ref. [1], to calculate $q_{\mathrm{B}} \approx -0.3$ at $\tau = 1\times10^{-5}$. Fluids with $q_{\mathrm{B}} < 0$ have larger acoustic attenuation than fluids with $q_{\mathrm{B}} = 0$. In the high-frequency limit ($\omega t_\xi \gg 1$), the bulk viscosity behaves as

$$\frac{i\omega\zeta(\omega)}{\rho c^2} = \frac{1+q_{\mathrm{B}}}{(i\omega t_\xi/2)^{-\alpha/\nu z} + q_{\mathrm{B}}} - 1, \tag{31}$$

where z is the dynamic exponent. The most accurate experimental value, which was determined from shear viscosity measurements in microgravity by Berg *et al.* [24], is $z - 3 = x_\eta \approx 0.0690 \pm 0.0006$. This value is in good agreement with the value 0.0679 ± 0.0007 recently calculated by Hao *et al.* using mode-coupling theory [25].

We estimate the bulk viscosity with the simple function

$$\frac{i\omega\zeta(\omega)}{\rho c^2} = \frac{1+q_{\mathrm{B}}}{(1+i\omega t_\xi/2)^{-\alpha/\nu z} + q_{\mathrm{B}}} - 1, \tag{32}$$

which smoothly interpolates between the low and high-frequency limits in Eqs. (29) and (31). The high-frequency limit of Eq. (32) agrees with Eq. (31). The low-frequency limit of Eq. (32) is

$$\frac{i\omega\zeta(0)}{\rho c^2} = \frac{\alpha}{2\nu z}\frac{i\omega t_\xi}{1+q_{\mathrm{B}}}, \tag{33}$$

which agrees with Eq. (29) if we replace R_{B} with $\alpha/(2z\nu) \approx 0.028$. This value of R_{B} is consistent with the ^{3}He experiments as mentioned earlier. Although Eq. (32) has the correct low- and high-frequency limits, it may not possess the correct dependence on ωt_ξ at intermediate frequencies. We hope that an accurate, theoretically based interpolation function for $\zeta(\omega)$ will be published in the future.

We observe that Eq. (32) gives precisely the bulk viscosity contribution to Δ_ν defined in Eq. (7). Using the dispersion relation in the critical region, Eq. (25), we can write Q^{-1} as (neglecting surface dissipation)

$$Q^{-1} = \frac{2\,\mathrm{Im}(\sqrt{1+i\Delta_\nu})}{\mathrm{Re}(\sqrt{1+i\Delta_\nu})}. \tag{34}$$

In the high-frequency limit of Eq. (31), Eq. (34) predicts that, as $T \to T_c$ at fixed frequency, the inverse quality factor Q^{-1} of a resonance (neglecting surface dissipation) reaches a temperature-independent, maximum value

$$Q^{-1}_{\max} = \frac{\pi\alpha/(2\nu z)}{1 + (B^+/A^+)(\omega t_0/2)^{\alpha/\nu z}}, \tag{35}$$

where $t_0 = \tau^{\nu z} t_\xi \approx 1.6\times10^{-12}$ s. For this work, $Q^{-1}_{\max}$ predicted by Eq. (35) is 0.128 for the Helmholtz mode and 0.140 for the $L5$ mode. The respective experimental values of Q^{-1} in the steel resonator at $\tau = 7\times10^{-6}$ were 0.124 and 0.155.

The frequency-dependent speed of sound in the critical region is, from Eqs. (9) and (25),

$$\frac{c(\omega)}{c} = \left[\mathrm{Re}\left(\frac{1}{\sqrt{1+i\Delta_\nu}}\right)\right]^{-1}. \tag{36}$$

The limiting behavior for $\omega t_\xi \gg 1$ as $T \to T_c$ is not temperature independent but has the form

$$\frac{c(\omega)}{c} \approx (\omega t_\xi/2)^{\alpha/\nu z}\left[\frac{1+q_{\mathrm{B}}}{1+(B^+/A^+)(\omega t_0/2)^{\alpha/\nu z}}\right]^{1/2}, \quad \omega t_\xi \gg 1. \tag{37}$$

Equation (37) predicts that $c(\omega)/c$ at $\tau = 7\times10^{-6}$ is 1.052 for the Helmholtz mode and 1.217 for the $L5$ mode. The respective experimental values of $c(\omega)/c$ in the steel resonator at $\tau = 7\times10^{-6}$ were 1.046 and 1.188.

To define the frequency-dependent specific heat, we substitute for q_{B} from Eq. (30) into Eq. (32),

$$1 + \frac{i\omega\zeta(\omega)}{\rho c^2} = \frac{C^*_V}{A^+\tau^{-\alpha}(1+i\omega t_\xi/2)^{-\alpha/\nu z} + B^+}, \tag{38}$$

where the background specific heat $B^+ \approx C^*_V - A^+\tau^{-\alpha}$. Following Onuki [9] and Ferrell and Bhattacharjee [7], we identify the denominator of Eq. (38) as the frequency-dependent specific heat $C^*_V(\omega)$. Thus, we write

$$1 + \frac{i\omega\zeta(\omega)}{\rho c^2} = \frac{C^*_V}{C^*_V(\omega)}, \tag{39}$$

where

$$C^*_V(\omega) = A^+\tau^{-\alpha}(1+i\omega t_\xi/2)^{-\alpha/\nu z} + B^+. \tag{40}$$

By inspection, $C^*_V(\omega)$ is obtained by replacing τ in C^*_V by $\tau(1+i\omega t_\xi/2)^{1/\nu z}$.

C. Calculation of resonance frequencies and half-widths

Two methods were used to calculate the resonance frequencies and quality factors for the modes of the resonator described in Sec. II. With the first method, we calculated the resonance frequency and quality factor directly from an analytic solution to the system of Eqs. (2) and boundary conditions (4). With the second method, we treated the effective surface admittance of the thermal and viscous boundary layers as a perturbation on the unperturbed eigenfunction, which included volume dissipation. Then we calculated the change in the wave number from the unperturbed case using first-order perturbation theory [22,26]. Both methods were used to calculate the resonance frequencies and quality factors for the longitudinal modes. The largest discrepancy in the resonance frequency between the two methods was about 0.05% at the lowest reduced temperature. The largest discrepancy in the quality factor was about 0.4%, also at the lowest reduced temperature. Only the second method was used to calculate the resonance frequency and quality factor for the Helmholtz mode.

Analytic solution for longitudinal modes

We analytically determined the resonance frequency f_{Ln} and quality factor Q_{Ln} of the nth longitudinal mode by first finding the standing wave solution to $\nabla^2\tilde{p}_{\rm ac}(\mathbf{r})=-k_{\rm ac}^2\tilde{p}_{\rm ac}(\mathbf{r})$ for the acoustic-wave pressure in a closed cylindrical chamber. Here, $\mathbf{r}$ is the position vector in cylindrical coordinates defined by the radial distance r, the azimuthal angle ϕ, and the axial position z. Then just enough of the thermal wave is added to the acoustic wave so that the total temperature $\tilde{T}=\tilde{T}_{\rm ac}+\tilde{T}_T$ satisfies boundary conditions (4c) and (4d). Finally, just enough of the shear wave, which solves $\nabla^2\tilde{\mathbf{u}}_{\rm vor}(\mathbf{r})=-k_{\rm v}^2\tilde{\mathbf{u}}_{\rm vor}(\mathbf{r})$, is added so that the total velocity $\tilde{\mathbf{u}}=\tilde{\mathbf{u}}_{\rm ac}+\tilde{\mathbf{u}}_T+\tilde{\mathbf{u}}_{\rm vor}$ satisfies boundary conditions (4a) and (4b). The composite solution that satisfies all the boundary conditions exists only for certain complex-valued eigenvalues K_n determined by the dimensions of the resonator. The complex frequency $\Omega/2\pi=f_{\rm r}+ig_{\rm r}$ that satisfies the resonance condition

$$k_{\rm ac}(\Omega)=\frac{\Omega}{c}q_-(\Omega)=K_n(\Omega) \tag{41}$$

gives the resonance frequency and half-width for driven oscillations. The general solution for all modes of a cylindrical resonator is described in detail in a forthcoming publication [27].

For the longitudinal modes of a cylindrical chamber with radius R and circular end plates at $z=0$ and $z=L$, the acoustic pressure is either antisymmetric or symmetric about the midplane $z=L/2$. The index n is odd for antisymmetric modes and even for symmetric modes. The acoustic pressure is proportional to the eigenfunction

$$\varphi_{Ln}=J_0(\alpha_{\rm ac}r)\sin[k_{\rm az}(z-L/2)]e^{i\omega t} \tag{42}$$

for the $n=1,3,5$ modes and

$$\varphi_{Ln}=J_0(\alpha_{\rm ac}r)\cos[k_{\rm az}(z-L/2)]e^{i\omega t} \tag{43}$$

for the $n=2$ and 4 modes, where

$$K_n^2=\alpha_{\rm ac}^2+k_{\rm az}^2. \tag{44}$$

The boundary conditions at the cylindrical wall and at the end plates yield two equations for each mode that, together with Eq. (44) for $K_n=k_{\rm ac}$, determine $\alpha_{\rm ac}$ and $k_{\rm az}$. The approximate equations, neglecting terms of order $(\delta_{\rm v}k_{\rm ac})^2$, $(\delta_{Ts}k_{\rm ac})^2$, and $|\delta_T k_{\rm ac}|^2$ are

$$2L_{\rm ac}=(k_{\rm az}R_T)^2F_{\rm v}+\frac{(k_TR_T)^2Yk_{Ts}G_{Ts}}{k_{Ts}G_{Ts}+\vartheta k_TF_T}F_T \tag{45}$$

and

$$ik_{\rm az}\cot\left(\frac{n\pi j_{\rm az}}{2k_{0n}}\right)=\frac{\alpha_{\rm ac}^2}{k_{\rm v}}+\frac{k_TY}{1+\vartheta}\quad (n\text{ odd}) \tag{46}$$

or

$$-ik_{\rm az}\tan\left(\frac{n\pi j_{\rm az}}{2k_{0n}}\right)=\frac{\alpha_{\rm ac}^2}{k_{\rm v}}+\frac{k_TY}{1+\vartheta}\quad (n\text{ even}), \tag{47}$$

where $\vartheta\equiv\lambda_Tk_T/(\lambda_{Ts}k_{Ts})$ and $Y\equiv-q_-^2(1-i\gamma\Delta_Tq_+^2)/[q_+^2(1-i\gamma\Delta_Tq_-^2)]$. We also define the function

$$F_{\rm v}\equiv\frac{2J_1(k_{\rm v}R_{\rm v})}{k_{\rm v}R_{\rm v}J_0(k_{\rm v}R_{\rm v})}, \tag{48}$$

$$F_T\equiv\frac{2J_1(k_TR_T)}{k_TR_TJ_0(k_TR_T)}, \tag{49}$$

$$L_{\rm ac}\equiv-\frac{\alpha_{\rm ac}RJ_1(\alpha_{\rm ac}R_T)}{J_0(\alpha_{\rm ac}R_T)}, \tag{50}$$

and

$$G_{Ts}\equiv-\frac{2H_1^{(2)}(k_{Ts}R_T)}{k_{Ts}R_TH_0^{(2)}(k_{Ts}R_T)} \tag{51}$$

in terms of the mth-order Bessel functions $J_m(x)$ and Hankel functions of the second kind $H_m^{(2)}(x)$. $F_{\rm v}$ and F_T are standard functions used to describe dissipative acoustics in circular ducts [28]. $L_{\rm ac}$ is proportional to the acoustic admittance of the acoustic wave at the wall of a circular duct (discussed in the next section). G_{Ts} is a measure of the thermal wave in the wall of a circular duct. The effective radii R_T and $R_{\rm v}$ are related to the geometric factors q_{Tn} and $q_{{\rm v}n}$ defined in Ref. [1], such that $R_T=1/q'_{Tn}$, $L_T=2/q''_{Tn}$, $q_{Tn}=q'_{Tn}+q''_{Tn}$, and $R_{\rm v}=1/q_{{\rm v}n}$. We have made the approximations $\sqrt{k_{\rm v}^2-k_{\rm az}^2}\approx\sqrt{k_{\rm v}^2-\alpha_{\rm ac}^2}\approx k_{\rm v}$, $\sqrt{k_T^2-k_{\rm az}^2}\approx\sqrt{k_T^2-\alpha_{\rm ac}^2}\approx k_T$, and $\sqrt{k_{Ts}^2-k_{\rm az}^2}\approx\sqrt{k_{Ts}^2-\alpha_{\rm ac}^2}\approx k_{Ts}$ which introduce small errors of order $(\delta_{\rm x}k_{\rm ac})^2\approx1\times10^{-5}$ or less in our frequency range.

In the absence of dissipation, $\alpha_{\rm ac}=0$ and $k_{\rm az}$ is determined by the zeros of the cotangent in Eq. (46) or tangent in Eq. (47). Even when the dissipation was strongest, $\alpha_{\rm ac}$ was only a few percent of $k_{\rm ac}$. Therefore, $\alpha_{\rm ac}$ is determined mostly by Eq. (45), since $k_{\rm az}\approx k_{\rm ac}$. Equations (46) and (47) are the conditions that determine the allowed values of $k_{\rm az}$.

In the dilute-gas limit, $i\Delta_Tq_+^2\approx1$ and $i\gamma\Delta_Tq_-^2\ll1$, so Eq. (45) reduces to

$$\alpha_{\rm ac}^2=-k_{\rm az}^2F_{\rm v}-k_{\rm ac}^2\frac{\gamma-1}{1+\vartheta}F_T, \tag{52}$$

where we have retained the parameter ϑ. In this limit, ϑ is just the ratio of the effusivity of xenon to the effusivity of the wall. If we combine Eqs. (44) and (52) and then eliminate $\alpha_{\rm ac}$, we obtain

$$k_{\rm az}=k_{\rm ac}\sqrt{\frac{1+\dfrac{\gamma-1}{1+\vartheta}F_T}{1-F_{\rm v}}}, \tag{53}$$

which is a generalization of the propagation parameter $\Gamma=ik_{\rm ac}$ for circular ducts [28] to include the finite effusivity of the walls. From the resonance condition (46) and (47), we obtain (for all $n>0$)

$$k_{az} \approx k_{0n}\left(1-(1-i)\frac{\gamma-1}{1+\vartheta}\frac{k_{ac}^2}{k_{0n}}\frac{\delta_T}{n\pi}\right) \tag{54}$$

and the total wave number

$$k_{ac} \approx k_{0n}\left(1-(1-i)\frac{\delta_v}{2R_v}-(1-i)\frac{\gamma-1}{1+\vartheta}\frac{\delta_T}{2R_T} -(1-i)\frac{\gamma-1}{1+\vartheta}\frac{k_{0n}\delta_T}{n\pi}\right). \tag{55}$$

Equation (55) reduces to the well-known result [29] if we set $R_v=R_T=R$ and $L=n\pi/k_{0n}$. We use the effective radii R_T and R_v and the effective length $L_{cal}=n\pi/k_{0n}$ to calibrate the dimensions of the resonator and take into account the imperfect geometry.

Since α_{ac} and k_{az} are implicit functions of ω, the root of Eq. (41) is found when ω in Eqs. (45)–(51) is replaced by the complex frequency $\Omega=2\pi(f_{Ln}+ig_{Ln})$. The resonance frequency and quality factor are then

$$f_{Ln}=\mathrm{Re}\left[\frac{c\sqrt{\alpha_{ac}^2+k_{az}^2}}{2\pi q_-}\right], \tag{56}$$

$$Q_{Ln}^{-1}=\frac{2g_{Ln}}{f_{Ln}}=\frac{2\,\mathrm{Im}[\sqrt{\alpha_{ac}^2+k_{az}^2}/q_-]}{\mathrm{Re}[\sqrt{\alpha_{ac}^2+k_{az}^2}/q_-]}. \tag{57}$$

Equations (56) and (57) include the effects of volume and surface dissipation. We can determine the individual contributions from surface and volume dissipation, since the volume dissipation is contained in q_-. If the surface dissipation were neglected, then the eigenvalue K_n would be real and Eq. (57) would reduce to

$$Q_{vol}^{-1}=\frac{2\,\mathrm{Im}(1/q_-)}{\mathrm{Re}(1/q_-)}=-\frac{2\,\mathrm{Im}(q_-)}{\mathrm{Re}(q_-)}, \tag{58}$$

which is just the volume loss in agreement with Eq. (10) since $\alpha_\lambda=\pi Q^{-1}$. If we set $q_-=1$ in Eq. (57) using the eigenvalue from Eqs. (45)–(47), which includes surface dissipation, then we get

$$Q_{surf}^{-1}=\frac{2\,\mathrm{Im}[\sqrt{\alpha_{ac}^2+k_{az}^2}]}{\mathrm{Re}[\sqrt{\alpha_{ac}^2+k_{az}^2}]}. \tag{59}$$

Note that Eqs. (57) and (59) include effects of bulk viscosity in the boundary layer.

2. Perturbation theory

The effect of the thermal and viscous boundary layers on the acoustic response of a resonator is the same to acoustic fields as if, instead of being rigid, the resonator's walls had a nonzero acoustic admittance per unit area β_{ac} such that

$$-\rho c\hat{\mathbf{n}}\cdot\tilde{\mathbf{u}}_{ac}(\mathbf{r}_w)=\beta_{ac}(\mathbf{r}_w)\tilde{p}_{ac}(\mathbf{r}_w), \tag{60}$$

where $\hat{\mathbf{n}}$ is the unit normal to the surface pointing into the gas and $\beta_{ac}(\mathbf{r}_w)$ is a function of position along the boundary. If we treat β_{ac} as a perturbation, we can calculate the eigenvalue with perturbation theory [22],

TABLE I. Values and uncertainties for some parameters used in the analysis. See also Tables VII and VIII in Ref. [1].

Parameter	Value
α	0.11±0.003[a]
ν	0.63±0.002[a]
y	0.04349±0.00035[b]
x_η	0.0690±0.0006[b]
P_c (MPa)	5.84[c]
ρ_c (kg m^{-3})	1116.0±1.7[d]
T_c (°C)	16.583±0.015[e]
ξ_o^+ (nm)	0.1866±0.001[e]
A^+	18.015±0.11[e]
B^+	−18.04±0.27[e]
C^+	0.42±0.1[e]
$\eta_o(T_c)$ (μPa s)	51.3±0.4[b]
$q_C\xi_o^+$	0.051±0.007[b]
$q_D\xi_o^+$	0.16±0.05[b]

[a]See Ref. [33].
[b]See Ref. [24].
[c]See Ref. [34].
[d]See Ref. [35].
[e]See Ref. [1].

$$k_n=k_{0n}+\frac{ik_{ac}}{2k_{0n}}\frac{\int_S\phi_{0n}^2(\mathbf{r}_s)\beta_{ac}(\mathbf{r}_s,f)dS}{\int_V\phi_{0n}^2(\mathbf{r})dV}, \tag{61}$$

where ϕ_{0n} is the eigenfunction (proportional to the pressure) satisfying $\nabla^2\phi_{0n}=-k_{0n}^2\phi_{0n}$ and the rigid-wall boundary condition (4a) only—i.e., zero surface admittance. The specific acoustic admittance $\beta_{ac}(\mathbf{r}_w)$ for a planar surface was given in Eq. (A31) of Ref. [1].

For a cylindrical resonator, we use the solution described in the previous section to obtain the specific acoustic admittance for the cylindrical wall β_{side},

$$\beta_{side}=\frac{\rho c\hat{\mathbf{r}}\cdot\tilde{\mathbf{u}}_{ac}(R)}{\tilde{p}_{ac}(R)}=\frac{1}{1-i\Delta_v q_-^2}\frac{ic}{\omega}\frac{L_{ac}}{R_T}, \tag{62}$$

and for the end plates β_{end},

$$\beta_{end}=\frac{\rho c(-\hat{\mathbf{z}})\cdot\tilde{\mathbf{u}}_{ac}(z=0)}{\tilde{p}_{ac}(z=0)}=\frac{\rho c\hat{\mathbf{z}}\cdot\tilde{\mathbf{u}}_{ac}(z=L)}{\tilde{p}_{ac}(z=L)} =\frac{1}{1-i\Delta_v q_-^2}\frac{c}{\omega}ik_{az}\cot\left(\frac{n\pi k_{az}}{2k_{0n}}\right)\quad(n\text{ odd}) =\frac{-1}{1-i\Delta_v q_-^2}\frac{c}{\omega}ik_{az}\tan\left(\frac{n\pi k_{az}}{2k_{0n}}\right)\quad(n\text{ even}). \tag{63}$$

The surface integrals in Eq. (61) are trivial since β_{side} and β_{end} are independent of position. For ϕ_{0n} we use Eq. (42) or (43) with $\alpha_{ac}=0$ and $k_{az}=k_{0n}$. The eigenvalue from Eq. (61) becomes

TABLE II. Results for the Helmholtz mode in the bare steel resonator. The resonance frequency f_r and quality factor Q_r were measured from the acoustic data. The speed of sound c_H was determined from the acoustic data using Eq. (79). Q_H was calculated from the model with Eq. (71).

τ	f_r (Hz)	Q_r^{-1}	ωt_ξ	Q_H^{-1}	c_H (m s^{-1})
7.66×10^{-6}	126.155	0.1237	7.427	0.1295	64.851
9.73×10^{-6}	126.897	0.1180	4.704	0.1198	65.223
1.11×10^{-5}	127.415	0.1139	3.655	0.1129	65.484
1.66×10^{-5}	129.275	0.1016	1.701	0.08762	66.437
2.53×10^{-5}	131.831	0.08809	0.7736	0.06606	67.788
3.73×10^{-5}	134.807	0.07813	0.3719	0.05672	69.405
5.49×10^{-5}	138.540	0.07083	0.1813	0.05499	71.458
8.05×10^{-5}	142.646	0.06568	0.0894	0.05707	73.752
1.17×10^{-4}	147.059	0.06239	0.0445	0.06055	76.256
1.71×10^{-4}	151.809	0.05985	0.0223	0.06333	78.990
2.48×10^{-4}	156.972	0.05697	0.0113	0.06276	81.951
3.59×10^{-4}	162.471	0.05370	5.70×10^{-3}	0.05806	84.955
5.20×10^{-4}	168.378	0.05004	2.90×10^{-3}	0.05228	87.990
6.87×10^{-4}	173.123	0.04689	1.75×10^{-3}	0.04805	90.355
9.94×10^{-4}	179.844	0.04205	8.94×10^{-4}	0.04259	93.658
1.44×10^{-3}	187.057	0.03715	4.58×10^{-4}	0.03730	97.183
2.08×10^{-3}	194.844	0.03222	2.36×10^{-4}	0.03230	100.990
3.00×10^{-3}	203.168	0.02773	1.21×10^{-4}	0.02772	105.073
4.34×10^{-3}	212.103	0.02368	6.27×10^{-5}	0.02366	109.480
6.28×10^{-3}	221.747	0.02026	3.25×10^{-5}	0.02016	114.263
9.08×10^{-3}	232.226	0.01732	1.69×10^{-5}	0.01719	119.492
1.31×10^{-2}	243.723	0.01486	8.80×10^{-6}	0.01472	125.257
1.90×10^{-2}	256.496	0.01281	4.62×10^{-6}	0.01267	131.691
2.74×10^{-2}	270.878	0.01110	2.43×10^{-6}	0.01098	138.961
3.61×10^{-2}	282.871	9.77×10^{-3}	1.51×10^{-6}	9.91×10^{-3}	145.037

$$k_n = k_{0n} + \frac{2}{L_T} i\beta_{\text{end}} + \frac{1}{R_T} i\beta_{\text{side}}, \tag{64}$$

from which the resonance frequency and quality factor are

$$f_{Ln} = \text{Re}\left[\frac{ck_n}{2\pi q_-}\right] \tag{65}$$

and

$$Q_{Ln}^{-1} = \frac{2\,\text{Im}[k_n/q_-]}{\text{Re}[k_n/q_-]}, \tag{66}$$

respectively.

A similar analysis for the Helmholtz mode gives the eigenvalue

$$k_H = k_{H0} + iq_T\beta_c + \frac{iV_d}{6V_c} q_v \beta_d, \tag{67}$$

where the specific acoustic admittances of the chamber and duct walls are

$$\beta_c = \frac{1+i}{1-i\Delta_v q_-^2} \frac{\omega}{2c} \frac{Yq_+^2}{1+\vartheta} \delta_T \tag{68}$$

and

$$\beta_d = \frac{1+i}{1-i\Delta_v q_-^2} \frac{\omega}{2c} \left(\frac{k_{az}}{k_{ac}}\right)^2 q_-^2 \delta_v + \frac{1+i}{1-i\Delta_v q_-^2} \frac{\omega}{2c} \frac{Yq_+^2}{1+\vartheta} \delta_T, \tag{69}$$

respectively, and the coefficients q_T and q_v were defined in [1]. The resonance frequency f_H and quality factor Q_H of the Helmholtz mode were determined by

$$f_H = \text{Re}\left[\frac{ck_H}{2\pi q_-}\right] \tag{70}$$

and

$$Q_H^{-1} = \frac{2\,\text{Im}[k_H/q_-]}{\text{Re}[k_H/q_-]}. \tag{71}$$

The working equations (65), (66), (70), and (71) include the effects of bulk viscosity.

In the first-order approximation, the inverse quality factor of the resonances Q^{-1} can be written as a sum of viscous

TABLE III. Results for the $L5$ mode in the bare steel resonator. The resonance frequency f_r and quality factor Q_r were measured from the acoustic data. The speed of sound c_{L5} was determined from the acoustic data using Eq. (79). Q_{L5} was calculated from the model with Eq. (66).

τ	f_r (Hz)	Q_r^{-1}	ωt_ξ	Q_{L5}^{-1}	c_{L5} (m s^{-1})
7.66×10^{-6}	3819.98	0.1552	224.9	0.1403	73.625
9.73×10^{-6}	3823.08	0.1510	141.7	0.1399	73.685
1.11×10^{-5}	3825.43	0.1482	109.7	0.1396	73.730
1.66×10^{-5}	3834.93	0.1382	50.45	0.1378	73.914
2.53×10^{-5}	3852.47	0.1249	22.61	0.1337	74.252
3.73×10^{-5}	3878.16	0.1100	10.70	0.1255	74.746
5.49×10^{-5}	3917.02	0.09278	5.127	0.1095	75.494
8.05×10^{-5}	3972.53	0.07501	2.489	0.08361	76.562
1.17×10^{-4}	4047.31	0.05822	1.224	0.05441	78.004
1.71×10^{-4}	4145.88	0.04301	0.6082	0.03307	79.912
2.48×10^{-4}	4264.29	0.03083	0.3057	0.02144	82.211
3.59×10^{-4}	4400.46	0.02185	0.1543	0.01595	84.867
5.20×10^{-4}	4551.18	0.01580	0.0784	0.01365	87.827
6.87×10^{-4}	4672.90	0.01274	0.0472	0.01263	90.232
9.94×10^{-4}	4845.62	9.93×10^{-3}	0.0241	0.01080	93.637
1.44×10^{-3}	5030.64	8.06×10^{-3}	0.0123	8.67×10^{-3}	97.222
2.08×10^{-3}	5230.06	6.65×10^{-3}	6.32×10^{-3}	6.98×10^{-3}	101.045
3.00×10^{-3}	5444.09	5.52×10^{-3}	3.25×10^{-3}	5.70×10^{-3}	105.136
4.34×10^{-3}	5674.45	4.60×10^{-3}	1.68×10^{-3}	4.69×10^{-3}	109.539
6.28×10^{-3}	5924.11	3.82×10^{-3}	8.68×10^{-4}	3.87×10^{-3}	114.316
9.08×10^{-3}	6196.57	3.18×10^{-3}	4.50×10^{-4}	3.20×10^{-3}	119.536
1.31×10^{-2}	6496.88	2.65×10^{-3}	2.35×10^{-4}	2.65×10^{-3}	125.296
1.90×10^{-2}	6831.74	2.21×10^{-3}	1.23×10^{-4}	2.21×10^{-3}	131.726
2.74×10^{-2}	7209.86	1.84×10^{-3}	6.47×10^{-5}	1.84×10^{-3}	138.991
3.61×10^{-2}	7527.34	1.62×10^{-3}	4.03×10^{-5}	1.62×10^{-3}	145.095

losses Q_η^{-1} and thermal losses Q_λ^{-1} at the boundaries of the resonator plus bulk losses Q_ζ^{-1} throughout the volume of the resonator:

$$Q^{-1} = Q_\eta^{-1} + Q_\lambda^{-1} + Q_\zeta^{-1}. \tag{72}$$

In [1], we derived approximate expressions for the losses in terms of the thermophysical properties and the frequency:

$$Q_\eta^{-1} \approx q_v \delta_v, \tag{73}$$

$$Q_\lambda^{-1} \approx (\gamma - 1) q_T \delta_T / (1 + \vartheta), \tag{74}$$

$$Q_\zeta^{-1} \approx \omega\zeta/(\rho c^2). \tag{75}$$

For each mode, the inverse lengths q_v and q_T are ratios of surface integrals to volume integrals defined in [1]. We estimated q_v and q_T by solving numerically the Helmholtz equation for the velocity potential for the modes H, $L1$, $L2$, and $L3$. For the $L4$ and $L5$ modes, we assumed that q_v and q_T had the values appropriate for a cylinder 48 nm long and 16 mm in diameter. As discussed in [1], these coefficients were adjusted slightly from the original estimates to improve the quality of the fit. The values for q_v and q_T and the unperturbed wave numbers k_0 used in this work were unchanged from the values tabulated in Tables IX and X from Ref. [1].

VI. ANALYSIS AND RESULTS

The resonance frequencies and half-widths were determined by the method described in Ref. [1]. The in-phase and quadrature voltages from the detector were fit with the standard resonance formula to determine the measured resonance frequency f_r and half-width g_r for each mode. The fitted parameters f_r and g_r were then corrected, as discussed in Ref. [1], to account for known systematic errors that grow as Q decreases. The errors arise because the standard resonance formula ignores the frequency dependence of the dissipation mechanisms that contribute to the half-width ($g_r \sim f^{-1/2}$ for surface losses and $\sim f$ for volume losses). We quantified these errors and developed corrections for them by fitting the standard resonance formula to numerical data generated by a model that included the frequency dependence of the losses, which we measured for xenon in the range $1\times10^{-3} < \tau < 7\times10^{-6}$. The largest corrections occurred close to T_c. For the Helmholtz mode, the corrections were $|\Delta f_r/f_r| \leqslant 0.4\%$ and $|\Delta Q/Q| \leqslant 1.7\%$. For the $L5$ mode they were $|\Delta f_r/f_r| \leqslant 0.5\%$ and $|\Delta Q/Q| \leqslant 0.4\%$.

TABLE IV. Results for the Helmholtz mode in the polymer-coated resonator. The measured f_r and quality factor Q_r were measured from the acoustic data. The speed of sound c_H was determined from the acoustic data using Eq. (79). Q_H was calculated from the model with Eq. (71).

τ	f_r (Hz)	Q_r^{-1}	ωt_ξ	Q_H^{-1}	c_H (m s^{-1})
7.94×10^{-6}	124.450	0.08385	6.837	0.1138	65.690
9.66×10^{-6}	125.008	0.07755	4.696	0.1045	65.998
1.17×10^{-5}	125.756	0.07051	3.246	0.09286	66.386
1.73×10^{-5}	127.533	0.05928	1.563	0.06521	67.332
2.48×10^{-5}	129.818	0.04712	0.7865	0.04252	68.545
3.59×10^{-5}	132.723	0.03623	0.3953	0.02815	70.085
5.21×10^{-5}	136.254	0.02737	0.1976	0.02022	71.955
7.52×10^{-5}	140.245	0.02005	0.1001	0.01614	74.068
1.09×10^{-4}	144.462	0.01711	0.0504	0.01400	76.299
1.58×10^{-4}	149.114	0.01480	0.0255	0.01290	78.761
2.28×10^{-4}	154.069	0.01336	0.0130	0.01229	81.382
3.29×10^{-4}	159.353	0.01256	6.61×10^{-3}	0.01193	84.177
4.76×10^{-4}	164.970	0.01207	3.37×10^{-3}	0.01171	87.147
6.89×10^{-4}	170.942	0.01173	1.72×10^{-3}	0.01153	90.305
9.95×10^{-4}	177.299	0.01141	8.78×10^{-4}	0.01135	93.665
1.44×10^{-3}	184.086	0.01116	4.50×10^{-4}	0.01116	97.251
2.08×10^{-3}	191.311	0.01089	2.31×10^{-4}	0.01094	101.067
3.01×10^{-3}	199.056	0.01058	1.19×10^{-4}	0.01069	105.155
4.34×10^{-3}	207.406	0.01027	6.13×10^{-4}	0.01041	109.559
6.28×10^{-3}	216.462	9.93×10^{-3}	3.17×10^{-5}	0.01008	114.332
9.08×10^{-3}	226.358	9.55×10^{-3}	1.64×10^{-5}	9.70×10^{-3}	119.543
1.31×10^{-2}	237.281	9.12×10^{-3}	8.58×10^{-6}	9.27×10^{-3}	125.290
1.90×10^{-2}	249.473	8.65×10^{-3}	4.51×10^{-6}	8.80×10^{-3}	131.702
2.74×10^{-2}	263.257	8.16×10^{-3}	2.40×10^{-6}	8.31×10^{-3}	138.948
3.59×10^{-2}	274.636	7.77×10^{-3}	1.53×10^{-6}	7.93×10^{-3}	144.931

Our model for the acoustic data requires, as inputs, the thermodynamic properties of near-critical xenon and the unperturbed wave number k_{0n} of the modes of each resonator. In Ref. [1], the thermodynamic properties were determined from our acoustic measurements in the range $1\times10^{-3}<\tau<0.04$ and from data from the literature. The results were expressed in algebraic forms that could be extrapolated towards T_c and we used these forms in this work. As described in Ref. [1], we determined k_{0n} from calibration with argon far from T_c, and we determined the effusivity of the polymer coating from the acoustic losses far from T_c. We emphasize that our model has no parameters that were adjusted to fit the present data in the range $1\times10^{-3}<\tau<7\times10^{-6}$.

The zero-frequency speed of sound c was calculated from the thermodynamic relation

$$c^2=\frac{\rho}{\chi_T}+\frac{T}{\rho^2 C_V}\left(\frac{\partial P}{\partial T}\right)_\rho^2. \tag{76}$$

In Eq. (76) we used the measured specific heat from Ref. [1], described by the scaling form

$$T_c\rho_c C_V/P_c=C_V^*=A^+\tau^{-\alpha}(1+C^+\tau^{0.5})+B^+, \tag{77}$$

with values for the parameters given in Table I, the isothermal susceptibility χ_T measured by Güttinger and Cannell [15], and $(\partial P/\partial T)_\rho$ from Swinney and Henry [17].

The thermal conductivity was calculated from Eq. (35) of Ref. [1]. The shear viscosity was calculated from the zero-frequency limit of Eq. (2) in Ref. [24],

$$\eta(T,\rho_c)=\eta_0(T,\rho_c)\exp[x_\eta H(q_C\xi,q_D\xi)], \tag{78}$$

which has the asymptotic dependence on ξ predicted by scaling. Equation (78) includes the crossover function H predicted by Bhattacharjee *et al.* [30] and the background viscosity from Ref. [31]. We used the values $x_\eta=0.069$, $q_C\xi_0=0.051$, and $q_D\xi_0=0.16$ determined experimentally in Ref. [24]. The background viscosity η_0 was scaled to be 51.3×10^{-6} Pa s at T_c as recommended by Berg *et al.* [24]. For the present work, the calculation of the relaxation time t_ξ, not the acoustic dissipation, required that we use a representation for the viscosity with the correct dependence on ξ.

The measured resonance frequencies and quality factors are tabulated for the H and $L5$ modes for the bare steel resonator in Tables II and III and for the polymer-coated resonator in Tables IV and V. These tables include predicted resonance frequencies calculated using Eqs. (56) and (70). The calculated dissipation in the polymer-coated resonator includes a small contribution from some exposed bare steel (about 5% of the area) where the flanges attach to the reso-

TABLE V. Results for the *L5* mode in the polymer-coated resonator. The measured f_r and quality factor Q_r were measured from the acoustic data. The speed of sound c_{L5} was determined from the acoustic data using Eq. (79). Q_{L5} was calculated from the model with Eq. (66).

τ	f_r (Hz)	Q_r^{-1}	ωt_ξ	Q_{L5}^{-1}	c_{L5} (m s^{-1})
7.94×10^{-6}	3837.13	0.1438	210.8	0.1399	73.754
9.66×10^{-6}	3839.83	0.1408	144.2	0.1393	73.806
1.17×10^{-5}	3843.73	0.1373	99.22	0.1385	73.882
1.73×10^{-5}	3854.79	0.1281	47.23	0.1361	74.096
2.48×10^{-5}	3870.93	0.1172	23.45	0.1319	74.407
3.59×10^{-5}	3895.15	0.1041	11.60	0.1240	74.874
5.21×10^{-5}	3932.37	0.08861	5.702	0.1093	75.591
7.52×10^{-5}	3984.10	0.07192	2.844	0.08580	76.588
1.09×10^{-4}	4053.07	0.05485	1.414	0.05682	77.917
1.58×10^{-4}	4146.15	0.03992	0.7102	0.03331	79.710
2.28×10^{-4}	4259.86	0.02716	0.3594	0.01889	81.900
3.29×10^{-4}	4392.12	0.01753	0.1823	0.01092	84.447
4.76×10^{-4}	4539.81	0.01097	0.0926	6.67×10^{-3}	87.290
6.89×10^{-4}	4700.85	6.92×10^{-3}	0.0472	4.44×10^{-3}	90.391
9.95×10^{-4}	4874.05	4.57×10^{-3}	0.0241	3.23×10^{-3}	93.725
1.44×10^{-3}	5059.09	3.26×10^{-3}	0.0124	2.57×10^{-3}	97.285
2.08×10^{-3}	5257.39	2.54×10^{-3}	6.35×10^{-3}	2.19×10^{-3}	101.100
3.01×10^{-3}	5469.84	2.12×10^{-3}	3.26×10^{-3}	1.96×10^{-3}	105.185
4.34×10^{-3}	5698.74	1.86×10^{-3}	1.68×10^{-3}	1.80×10^{-3}	109.586
6.28×10^{-3}	5946.84	1.67×10^{-3}	8.71×10^{-4}	1.68×10^{-3}	114.355
9.08×10^{-3}	6217.75	1.53×10^{-3}	4.52×10^{-4}	1.56×10^{-3}	119.561
1.31×10^{-2}	6516.69	1.41×10^{-3}	2.36×10^{-4}	1.45×10^{-3}	125.305
1.90×10^{-2}	6850.32	1.29×10^{-3}	1.24×10^{-4}	1.33×10^{-3}	131.714
2.74×10^{-2}	7227.44	1.18×10^{-3}	6.60×10^{-5}	1.21×10^{-3}	138.958
3.59×10^{-2}	7538.90	1.10×10^{-3}	4.20×10^{-5}	1.13×10^{-3}	144.941

nator. The measured and modeled dissipation (Q^{-1}) as functions of the reduced temperature are shown in Fig. 9 for the *H* and *L5* modes in both resonators. Four reduced temperatures, where $\varepsilon_{Xe}=\varepsilon_{steel}$, $\varepsilon_{Xe}=\varepsilon_{polymer}$, $\gamma\omega t_\xi=1$, and $\omega t_\xi=1$, are indicated in the figure. Thermal and shear losses at the surface dominate the dissipation for temperatures to the right of the line $\gamma\omega t_\xi=1$ in the figure. The surface losses saturate in the vicinity of $\varepsilon_{Xe}=\varepsilon_{steel}$ and $\varepsilon_{Xe}=\varepsilon_{polymer}$ for the respective resonators. The energy loss in the fluid volume due to bulk viscosity dominates the dissipation for temperature to the left of the line $\omega t_\xi=1$.

The model agrees with the data at the highest reduced temperatures where the influence of the bulk viscosity is negligible and at the lowest reduced temperatures where the dissipation is dominated by the bulk viscosity acting throughout the volume of resonator. The largest differences between the model and the data occur for the *H* mode of steel resonator. As T_c is approached from the temperature where $\gamma\omega t_\xi=1$, the modeled dissipation rises above the experimental values and then drops below the experimental values. The largest difference for the Helmholtz mode is a factor of 1.4; the factor decreases as the frequency increases. The differences are largest where the effect of the bulk viscosity on the boundary layer peaks, as predicted by the model. The peak in the boundary layer dissipation of the polymer resonator is much smaller than the corresponding peak for the steel resonator because the effusivity of the polymer is much smaller than the effusivity of the steel.

The model predicts that the bulk viscosity "stiffens" the thermal boundary layer, thereby lowering the thermal boundary layer admittance from what it would be if bulk viscosity were not present. To demonstrate this, we repeated the calculations with the bulk viscosity contributing only to the volume dissipation and plotted the results as the dash-dotted curves (labeled $\zeta_{surf}=0$) in Fig. 9. The $\zeta_{surf}=0$ curves do not have the inflections that the theory predicts for the dissipation in the steel resonator; however, the total dissipation at the lowest temperature is larger for the $\zeta_{surf}=0$ curves due to the higher boundary layer admittance. For the polymer-coated resonator, omitting the bulk viscosity from the surface dissipation made a negligible difference from the theory. We emphasize that the $\zeta_{surf}=0$ calculation is *ad hoc*; we have no physical reason to omit the bulk viscosity from the boundary layer.

The frequency-dependent speed of sound $c(\omega)$ was determined as a function of temperature for each mode from the measured resonance frequency, the corrections for the known perturbations, and the mode's unperturbed wave number k_{0n}.

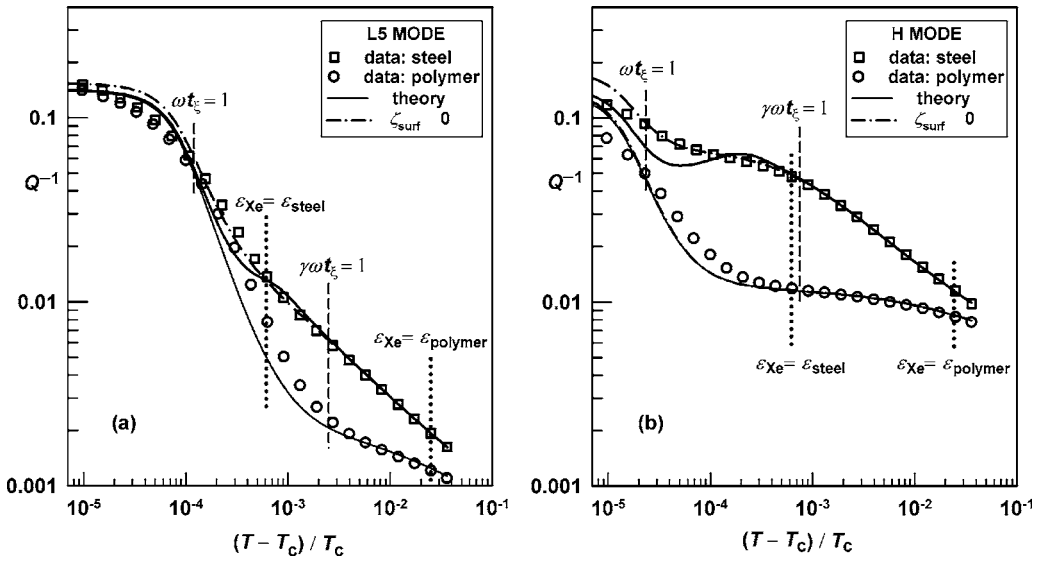

FIG. 9. The dissipation Q^{-1} as a function of reduced temperature for (a) the fifth longitudinal mode, $L5$, and (b) the Helmholtz mode, H. In both graphs, the symbols denote measurements in the steel □ and polymer-coated ○ resonators. The solid curves are calculated from Eqs. (57) and (71) for the $L5$ and H modes, respectively. The dash-dotted curves are the predicted losses when the bulk viscosity is included only in the volume dissipation ($\zeta_{surf}=0$).

$c(\omega)$ is calculated from the measured resonance frequency according to

$$c(\omega) = \frac{2\pi f_{meas}}{\mathrm{Re}(k_n)} \approx \frac{2\pi(f_{meas} - \Delta f)}{k_{0n}}, \tag{79}$$

where $\Delta f = (c/2\pi)\mathrm{Re}[k_n - k_{0n}]$ is the predicted frequency shift due to the presence of the boundary layer (estimated from perturbation theory). The speed-of-sound data is shown in Fig. 10 where the phase velocity for the H and $L5$ modes is plotted as a function of reduced temperature. For $\omega t_\xi < 1$ the speed of sound for the $L5$ and H modes agrees with the zero-frequency speed of sound as expected from dynamic scaling. For $\omega t_\xi > 1$, the difference between the $c(\omega)$ and c increases with increasing frequency. At $\tau = 7 \times 10^{-6}$, the measured $c(\omega)$ is within 0.6% of the predicted value for the Helmholtz mode and within 2% of the predicted value for the $L5$ mode.

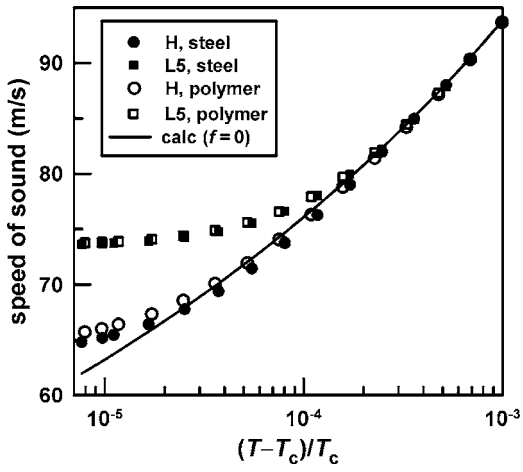

FIG. 10. The speed of sound as a function of reduced temperature deduced from the Helmholtz modes (circles) and $L5$ modes (squares) in the bare steel resonator (solid symbols) and polymer-coated resonator (open symbols). The dispersion is evident when $\omega t_\xi > 1$. The solid curve is the zero-frequency speed of sound from Eq. (76).

The ratio $c(\omega)/c$ was calculated using the values of c from Eq. (76). Figure 11(a) displays $c(\omega)/c$ as a function of ωt_ξ for both resonators. At large values of ωt_ξ, the dispersion of in the speed of sound approaches 20% in our data. Figure 11(b) displays the ratios of the experimental to calculated phase velocities $c(\omega)/c(\omega)_{calc}$ for the steel and polymer-coated resonators. The calculated phase velocities differ from the measurements by at most 2.2%. The differences are a smooth function of ωt_ξ with a peak near $\omega t_\xi \approx 1$. However, the deviations are not a smooth function of the reduced temperature, as shown in Fig. 11(c). Because the bulk viscosity is the property in our model that has the strongest variation with ωt_ξ, we speculate that a better model for $\zeta(\omega)$ would reduce the differences. We are currently investigating ways to deduce $\zeta(\omega)$ directly from our dissipation and dispersion measurements. However, because $\zeta(\omega)$ is a complex-valued function that must satisfy Kramers-Kronig relations, this is not a trivial matter. This work will be the subject of a forthcoming article.

In Fig. 11(b), the data from the polymer-coated resonator are more tightly clustered than the data from the steel resonator and, on the average, are at higher values of $c(\omega)/c(\omega)_{calc}$. We suspect that these features have two causes. First, the dissipation in the boundary layer is much higher in the steel resonator than in the polymer-coated resonator. Second, as discussed below, our model for the dissipation in the boundary layer overestimates the boundary losses for the steel resonator.

The dispersion and attenuation of ultrasound in near-critical xenon were measured by Garland and collaborators

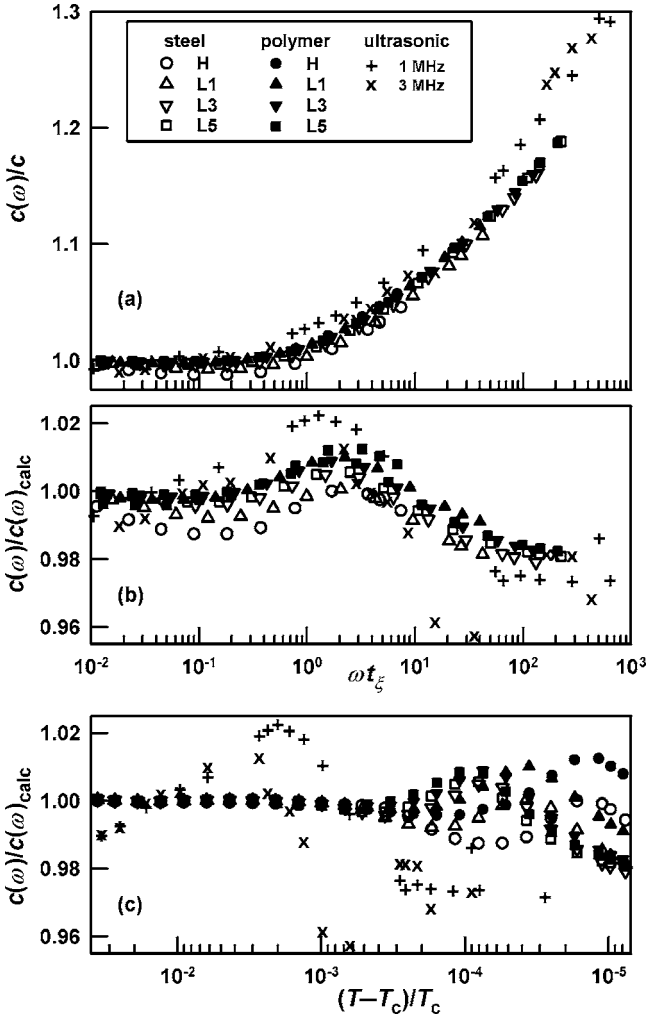

FIG. 11. (a) The ratio of the measured speed of sound at frequency ω to the thermodynamic (zero-frequency) speed of sound as a function of ωt_ξ. The data from the steel resonator are denoted by open symbols; the data from the polymer coated resonator denoted by solid symbols. The ultrasonic data ($\times$ and $+$) are from Ref. [2]. We calculated the zero-frequency speed of sound c from Eq. (76). (b) Ratio of the experimental to calculated speeds of sound as a function of ωt_ξ. We calculated $c(\omega)_{\rm calc}$ from Eq. (9) using the bulk viscosity from Eq. (32) with no adjusted parameters. (c) Same as (b), but plotted as a function of $(T-T_c)/T_c$. Note that the horizontal axis in (c) is reversed.

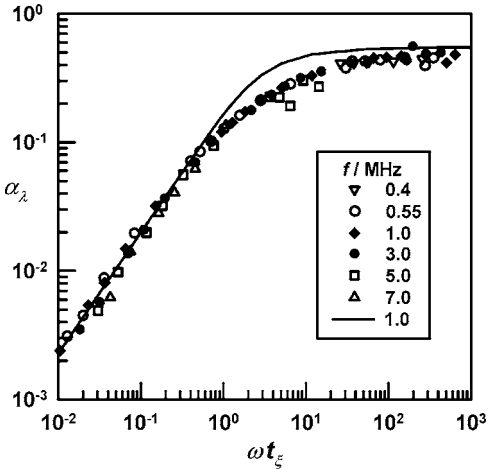

FIG. 12. The ultrasonic attenuation α_λ from Ref. [2] as a function of ωt_ξ. Before plotting, we multiplied the values by Eq. (80) as recommended in Ref. [3]. The curve is the calculated attenuation at 1 MHz from Eq. (10) using the bulk viscosity from Eq. (32) with no adjusted parameters. The attenuation from shear viscosity and thermal conductivity have been omitted from the experimental and calculated values.

in the 1970s [2,3]. They used an interferometer to measure $c(\omega)$ and the attenuation per wavelength, α_λ, in a comparatively large, geometrically complicated, stirred cell. They reported difficulties in dealing with density gradients near T_c. In Ref. [2], Garland's group tabulated values of $c(\omega)$ and α_λ measured along the isochore with density 1.01 ρ_c for frequencies in the range 0.4 MHz$<f<$7 MHz. We include in Fig. 11 $c(\omega)$ at 1 MHz and 3 MHz as tabulated in Ref. [2]. In Fig. 11(a), the ultrasonic data for $\omega t_\xi \gg 1$ show a higher dispersion than our audio frequency data at the same ωt_ξ; this is predicted by the theory [9]. Figure 11(b) shows that the ultrasonic data nearly agree with the present model, without adjusting any parameters. It is remarkable that data spanning a frequency ratio of (3 MHz)/(120 Hz)=25 000 are so nearly consistent. Furthermore, the ultrasonic data deviate from our model smoothly as a function of ωt_ξ with a broad peak at $\omega t_\xi \approx 1$. Because the ultrasonic data were not acquired with a resonator, they are not influenced by dissipation in boundary layers. This supports our speculation that a better function is needed for $\zeta(\omega)$.

Figure 11(c) shows that there is a systematic difference between the present speed-of-sound data and the ultrasonic data in the temperature range $3\times10^{-2}>(T-T_c)/T_c>1\times10^{-3}$. We have no explanation for this. (As discussed in Ref. [1], the present speed-of-sound data are within 0.2% of the data of Kline and Carome far above T_c [32].)

In a subsequent publication, Thoen and Garland [3] state that gravity had caused temperature-dependent density changes such that the tabulated attenuation data[2] in Ref. [2] "are low by about 15% near T_c" and that this phenomenon occurred when $\omega t_\xi \geqslant 2$. In accordance with this, we multiplied the tabulated values of α_λ from Ref. [2] by the factor

$$A + B\tanh[\ln(\omega t_\xi/2)], \tag{80}$$

with $A=1.0882$ and $B=0.0882$, which smoothly crosses over from 1 to 1.18 near $\omega t_\xi=2$. In Fig. 12, the corrected measurements are compared with the values calculated for 1 MHz using Eq. (10) together with the thermodynamic and transport properties of xenon used in the analysis of the present data. No empirical parameters were adjusted for this comparison. For $\omega t_\xi \ll 1$, the measured and calculated values of α_λ agree within the scatter of the data. Near $\omega t_\xi \approx 5$, the measured values of α_λ are 2/3 of the calculated values, and for $\omega t_\xi \gg 1$, the measured values of α_λ are approximately

[2]Thoen and Garland state that gravity did not noticeably affect the ultrasonic velocity data $c(\omega)$; therefore, we used these data as tabulated.

88% of the calculated values. We speculate that the agreement between the ultrasonic measurements and the theory could be improved near $\omega t_\xi \approx 5$ by using a better functional form for $\zeta(\omega)$. Perhaps the measurement problems in the region $\omega t_\xi \gg 1$ were not fully accounted for by the factor of 1.18 recommended by Thoen and Garland.

VII. CONCLUSIONS

The data from the stirred samples (Figs. 3–5) indicate that the useful temperature resolution of the stirred samples is on the order of a few millikelvin. We estimate that the condition $\omega t_\xi = 1$ was encountered for the H mode at the reduced temperature $\tau \approx 2.3 \times 10^{-5}$ and $f_H \approx 131$ Hz and for the $L1$ mode at $\tau \approx 5.5 \times 10^{-5}$ and $f_{L1} \approx 758$ Hz and for the $L5$ mode at $\tau \approx 1.3 \times 10^{-4}$ and $f_{L5} \approx 4070$ Hz. In previous experiments at megahertz frequencies, $\omega t_\xi = 1$ occurred much further from T_c. Thus, a convectively stirred sample can be used for low-frequency tests of dynamic scaling much closer to T_c than an isothermal sample.

Our theory for the resonator, which includes the effects of bulk viscosity, predicts dissipation that agrees within a factor of 1.4 or less with measurements in both the bare steel and polymer-coated resonators. The predicted frequency dependence of the speed of sound agrees within 2% with experimental values. The theory predicts peaks in the temperature dependence of the dissipation in the steel resonator that are not observed. A calculation which omits the bulk viscosity from the boundary layer suggests that the effect of the bulk viscosity on the surface dissipation is weaker in the experiment than the theory predicts. We considered four possible explanations for this discrepancy. First, an unexpected temperature distribution might exist within the xenon due to the applied temperature gradient. Perhaps this temperature distribution differs in the two resonators because the thermal properties of the polymer coating and the bare steel are very different. However, the results were independent of the size of the applied temperature gradient (Figs. 4 and 5). Second, upon disassembling other resonators coated with the same polymer, we found instances where the polymer coating partially separated from the steel substrate leaving voids that would fill with xenon. In these cases, the measured dissipation was anomalously large. Perhaps a version of this phenomenon explains why the dissipation in the polymer-coated resonator was larger than expected and the fitted effusivity of the polymer was larger than estimated from its properties [1]. Third, the approximate expression that we used for the bulk viscosity, Eq. (32), may not be good enough. The deviations between the model and data were found to be sensitive to the interpolation function used for $\zeta(\omega)$. A full calculation of the bulk viscosity integral is necessary in order to fully assess the ability of the model to correctly predict the dispersion and the dissipation. Fourth, our fundamental assumption that we can use linear hydrodynamics and include the dynamic scaling effects in the bulk viscosity as predicted by others may be incorrect. We did search for nonlinear hydrodynamic effects; however, we did not find any.

ACKNOWLEDGMENTS

We thank Ron Morris of ZIN Technologies, Inc. for calculating the temperature distribution within the thermostat and the resonator. We thank Mikhail Anisimov (University of Maryland), James Mehl, and Bobby Berg of NIST for their suggestions. This research was supported, in part, by NASA Contract No. C-32088-K.

[1] K. A. Gillis, I. I. Shinder, and M. R. Moldover, Phys. Rev. E **70**, 021201 (2004).
[2] P. E. Mueller, D. Eden, C. W. Garland, and R. C. Williamson, Phys. Rev. A **6**, 2272 (1972).
[3] Jan Thoen and Carl W. Garland, Phys. Rev. A **10**, 1311 (1974).
[4] A. B. Kogan and H. Meyer, J. Low Temp. Phys. **110**, 899 (1998); D. B. Roe and H. Meyer, *ibid.* **30**, 91 (1978); T. Doiron, D. Gestrich, and H. Meyer, Phys. Rev. B **22**, 3202 (1980).
[5] A. V. Voronel, in *Phase Transitions and Critical Phenomena*, edited by C. Domb and M. S. Green (Academic Press, New York, 1976), Vol. 5B, Chap. 5; M. I. Bagatskii, A. V. Voronel', and V. G. Gusak, Zh. Eksp. Teor. Fiz. **43**, 728 (1962) [Sov. Phys. JETP **16**, 517 (1963)].
[6] D. S. Cannell, Phys. Rev. A **12**, 225 (1975).
[7] R. A. Ferrell and J. K. Bhattacharjee, Phys. Lett. **86A**, 109 (1981); Phys. Rev. A **31**, 1788 (1985); J. K. Bhattacharjee and R. A. Ferrell, *ibid.* **24**, R1643 (1981).
[8] R. Folk and G. Moser, Phys. Rev. E **57**, 683 (1998); **57**, 705 (1998).
[9] Akira Onuki, Phys. Rev. E **55**, 403 (1997); Akira Onuki, *Phase Transition Dynamics* (Cambridge University Press, Cambridge, England 2002), Chap. 6.
[10] In order to describe materials and experimental procedures adequately, it is occasionally necessary to identify commercial products by the manufacturer's name or label. In no instance does such identification imply endorsement by the National Institute of Standards and Technology; nor does it imply that the particular product or equipment is necessarily the best available for the purpose.
[11] The thermophysical properties of Parylene C were provided by the manufacturer, except for the effusivity, which came from Ref. [1].
[12] K. A. Gillis, J. B. Mehl, and M. R. Moldover, Rev. Sci. Instrum. **67**, 1850 (1996).
[13] P. C. Hohenberg and M. Barmatz, Phys. Rev. A **6**, 289 (1972).
[14] M. R. Moldover, J. V. Sengers, R. W. Gammon, and R. J. Hocken, Rev. Mod. Phys. **51**, 79 (1979).
[15] The susceptibility on the critical isochore above T_c measured by Hannes Güttinger and D. S. Cannell, Phys. Rev. A **24**, 3188 (1981). See Table VII in Ref. [1] for the expression and values of coefficients.
[16] The heat capacity on the critical isochore above and below T_c was measured by C. Edwards, J. A. Lipa, and M. J. Buckingham, Phys. Rev. Lett. **20**, 496 (1968) and reanalyzed by Güttinger and Cannel [15].

[17] $(\partial P/\partial T)_\rho$ on the critical isochore above T_c from the pressure-temperature data of H. W. Habgood and W. G. Schneider, Can. J. Chem. **32**, 98 (1954) and analyzed by H. L. Swinney and D. L. Henry, Phys. Rev. A **8**, 2566 (1973). See Table VII in Ref. [1] for the expression and values of coefficients.

[18] The speed of sound on the critical isochore above and below T_c measured by Garland and Williams and Thoen and Garland. See Ref. [2].

[19] M. Gitterman and V. Steinberg, High Temp. **8**, 754 (1971); M. Gitterman, Rev. Mod. Phys. **50**, 85 (1978).

[20] P. Carles and B. Ugurtas, Physica D **126**, 69 (1999).

[21] R. F. Berg, G. A. Zimmerli, and M. R. Moldover, Int. J. Thermophys. **19**, 481 (1998).

[22] P. M. Morse and K. U. Ingard, *Theoretical Acoustics* (McGraw-Hill, New York, 1968).

[23] J. Bhattacharjee and R. A. Ferrell, Phys. Lett. **76A**, 290 (1980); Phys. Rev. A **27**, 1544 (1983).

[24] R. F. Berg, M. R. Moldover, and G. A. Zimmerli, Phys. Rev. E **60**, 4079 (1999). See also R. F. Berg, M. R. Moldover, and G. A. Zimmerli, Phys. Rev. Lett. **82**, 920 (1999).

[25] H. Hao, R. A. Ferrell, and J. K. Bhattacharjee, Phys. Rev. E **71**, 021201 (2005).

[26] J. B. Mehl and M. R. Moldover, J. Chem. Phys. **74**, 4062 (1981).

[27] K. A. Gillis (unpublished).

[28] K. A. Gillis, J. B. Mehl, and M. R. Moldover, J. Acoust. Soc. Am. **114**, 166 (2003).

[29] J. P. M. Trusler, *Physical Acoustics and Metrology of Fluids* (Adam Hilger, Bristol, 1991).

[30] J. K. Bhattacharjee, R. A. Ferrell, R. S. Basu, and J. V. Sengers, Phys. Rev. A **24**, 1469 (1981).

[31] R. F. Berg and M. R. Moldover, J. Chem. Phys. **93**, 1926 (1990).

[32] J. L. Kline and E. F. Carome, J. Chem. Phys. **58**, 4962 (1973).

[33] V. A. Agayan, M. A. Anisimov, and J. V. Sengers, Phys. Rev. E **64**, 026125 (2001).

[34] J. V. Sengers and J. M. H. Sengers, Annu. Rev. Phys. Chem. **37**, 189 (1986).

[35] U. Närger and D. A. Balzarini, Phys. Rev. B **42**, 6651 (1990).